



HAL
open science

Controls on overpressure evolution during the gravitational collapse of the Amazon deep-sea fan

Juliana Maria Gonçalves Souza, Nadaya Cubas, Claudio Rabe, Jean Letouzey, Renaud Divies, Daniel Praeg, Didier Granjeon, Alberto Machado Cruz, Cleverson Guizan Silva, Antonio Tadeu dos Reis, et al.

► To cite this version:

Juliana Maria Gonçalves Souza, Nadaya Cubas, Claudio Rabe, Jean Letouzey, Renaud Divies, et al.. Controls on overpressure evolution during the gravitational collapse of the Amazon deep-sea fan. *Marine and Petroleum Geology*, 2020, 121, pp.104576. 10.1016/j.marpetgeo.2020.104576 . hal-03117839

HAL Id: hal-03117839

<https://ifp.hal.science/hal-03117839>

Submitted on 22 Jan 2021

HAL is a multi-disciplinary open access archive for the deposit and dissemination of scientific research documents, whether they are published or not. The documents may come from teaching and research institutions in France or abroad, or from public or private research centers.

L'archive ouverte pluridisciplinaire **HAL**, est destinée au dépôt et à la diffusion de documents scientifiques de niveau recherche, publiés ou non, émanant des établissements d'enseignement et de recherche français ou étrangers, des laboratoires publics ou privés.

Controls on overpressure evolution during the gravitational collapse of the Amazon deep-sea fan

Juliana Maria Gonçalves de Souza^{a*}, Nadaya Cubas^a, Claudio Rabe^b, Jean Letouzey^a, Renaud Divies^c, Daniel Brian Praeg^{b,d}, Didier Granjeon^c, Alberto Machado Cruz^a, Cleverson Guizan Silva^b, Antonio Tadeu dos Reis^b, Christian Gorini^a.

^a Institut des Sciences de la Terre de Paris, Sorbonne Université. 4 Place Jussieu, 75005 Paris, France.

^b Departamento de Geologia - Lagamar, Universidade Federal Fluminense (UFF). Av.

Litorânea, s/n, Boa Viagem, Niterói, RJ, CEP: 24210 - 346, Brazil.

^c IFP Energies Nouvelles. 1 - 4 avenue de Bois - Préau, 92852 Rueil-Malmaison, France.

^d Géoazur (UMR7329 CNRS), 250 Rue Albert Einstein, Valbonne, France

***Corresponding author (juliana.goncalvesuff@gmail.com)**

Abstract

The Amazon Fan provides a natural laboratory to study the generation of overpressure, due to rapid late Cenozoic burial that has resulted in gravitational collapse above shale detachments. Here we examine collapse systems for the first time using the techniques of petroleum systems analysis. We propose an integrated methodology based on numerical modeling constrained by the structural restoration of a seismic profile across the southwestern fan. The results provide information on the evolution of pore pressure and temperature and their implications for the operation of the detachment and overlying extensional and compressional faults during the deposition of up to 6 km of sediment over the last 8 Ma. The modeled thermal history implies that fluid release by smectite-to-illite transformation has taken place within the thickening sedimentary succession, but has not significantly contributed to pore pressures along the detachment. Modeling of hydrocarbon generation and migration from source rocks beneath the fan indicates gas accumulated in successions at depths of 10^2 - 10^3 m beneath the detachment without influencing pore pressures along it. In contrast, model results indicate that overpressures have varied in response to disequilibrium compaction. Fault activity within the collapse system took place during phases of higher sedimentation rates, and ceased from 5.5-3.7 Ma when sediment supply to the SE fan decreased. From 2 Ma, renewed sediment flux and shelf-slope progradation led to a basinward migration both of overpressure along the detachment and of fault activity above it. We conclude that gravity tectonics in the Amazon Fan over the last 8 Ma have been mainly controlled by overpressures due to disequilibrium compaction, with secondary contributions from clay mineral transformation. Present-day pressure conditions show that the southeastern Amazon Fan is not at equilibrium and gravity driven deformation could occur at any time.

Keywords: overpressure evolution, overpressure mechanism, gravitational collapse, basin and mechanical modeling, Amazon Fan

V.1 INTRODUCTION

Excess pore fluid pressure plays a key role in the stability of continental slopes, through its influence on the strength of sedimentary successions during their deposition. Burial and consolidation generally lead to an increase in sediment strength, but this first-order process can be temporarily reversed by variations in permeability and/or loading leading to the development of overpressures (e.g. [Maltman and Bolton, 2003](#)). Overpressure, defined as any pressure that exceeds the hydrostatic pressure of a column of water or formation brine, leads to variations in sediment strength that may lead to formation failure ([Dickinson, 1953](#)). Overpressured fluids are particularly important in the mobilization of fine-grained sediments and play a fundamental role in gravity-driven processes of sediment failure and deformation on continental slopes ([Bolton et al., 1998](#)), and in the operation of syn-sedimentary faults as well as the stability of wellbores ([Moos et al., 2003](#)). Hence, pore pressure is an issue of major concern for both our understanding of continental margin evolution and hydrocarbon exploitation ([Morley et al., 2011](#)).

Mechanisms generating overpressures in sedimentary successions can be divided into those related to external stresses or those that increase internal fluid content. Stress-related processes include (1) regional tectonics, and (2) disequilibrium compaction (undercompaction), the latter being most common in deltaic depositional environments with high sedimentation rates ([Osborne and Swarbrick, 1997](#); [Burrus, 1998](#); [Law and Spencer, 1998](#); [Nashaat, 1998](#); [Swarbrick and Osborne, 1998](#); [Grauls, 1999](#); [Zoback, 2007](#)). Increased fluid content can be generated by processes that depend on pressure and temperature, either (3) clay diagenesis, such as the smectite-illite transition ([Hower et al., 1976](#); [Law et al., 1983](#); [Bruce, 1984](#); [Hall, 1993](#); [Burrus, 1998](#); [Swarbrick and Osborne, 1998](#); [Bowers, 2001](#)), or (4) hydrocarbon generation. In the latter case, volume changes occur when kerogen transforms to oil and gas (primary migration) and oil cracks to gas (secondary migration), but only gas is

able to generate significant overpressures (Law and Spencer, 1998; Swarbrick and Osborne, 1998; Grauls, 1999).

The post-rift successions of many passive continental margins are affected by gravity tectonics, in which a sediment volume moves downslope above one or more zones of decollement containing detachment surfaces. The gravitational potential is directly proportional to the slope of the seafloor and the properties of the detachment surface (Vendeville and Cobbold, 1987; Cobbold et al., 1989). Deformation of the succession above the detachment surface typically results in an upslope extensional domain and a downslope compressional domain similar to a fold-and-thrust belt (Rowan et al., 2004). Gravitational collapse can be related to the presence beneath a sedimentary succession of ductile evaporites (e.g. Morley & Guerin, 1996), but on many margins it has been shown to be linked to the presence of overpressured shale levels, such as the Niger Delta (Morley & Guerin, 1996; Hooper et al., 2002; Morley et al., 2011; Wu et al., 2015), the northwestern Gulf of Mexico (Rowan et al., 2004), the Brunei margin (Berthelon et al., 2018) or the Amazon Fan (Cobbold et al., 2004; Oliveira, 2005; Morley et al., 2011; Perovano et al., 2011).

Shale detachments form in response to pore fluid overpressures, which depend on factors including sediment loading, burial and deformation history, and the production and migration of thermogenic fluids (Morley & Guerin, 1996; Cobbold et al., 2004; Rowan et al., 2004; Mourgues et al., 2009; Ings & Beaumont, 2010; Oliveira et al 2011). The origin of shale detachments was reviewed by Morley et al. (2011). According to these authors, the main cause of overpressures within weak shale successions is disequilibrium compaction induced by high sedimentation rates and deep burial, enhanced by possible inflationary overpressure mechanisms resulting from diagenesis during burial. These results were mainly based on analogue mechanical models, which assumed the origin and type of overpressured fluids. While such studies have clearly identified the need to consider overpressure along detachment surfaces (e.g. Shaw and Bilotti, 2005; Yuan et al., 2017, 2020; Berthelon et al.,

2018), none have integrated basin pore pressure evolution or modelled the possible origins of fluid pressures within the basin and along the detachment.

The Amazon River has one of the world's largest discharges of suspended sediment (Meade, 1994) and culminates in one of its largest deep-sea fans (Fig. 5.1), comparable in size to those of the Bengal, Indus and Mississippi rivers (Rimington et al., 2000). Onshore to offshore studies indicate that the trans-continental Amazon River has developed since the mid-Miocene in response to Andean uplift (Hoorn et al., 1995, 2010, 2017), resulting in the progradation of a shelf-slope depocentre up to 10 km thick (Silva et al., 1999; Watts et al., 2009). Stratigraphic studies of the Amazon fan based on seismic and well data indicate that sediment flux to the Amazon offshore increased through time to reach a maximum during the Quaternary, i.e. the last 2.6 Ma (Figueiredo et al., 2009; Cruz et al., 2019). Seismic data also show that the growth of the fan has been accompanied by its gravitational collapse, expressed as linked extensional-compressional fault systems rooted on detachment surfaces up to hundreds of kilometers in extent at subsurface depths of up to 10km (Silva et al., 1999; Cobbold et al., 2004; Oliveira, 2005; Perovano et al., 2009, 2011). Three main detachment surfaces have been recognized within the Upper Cretaceous to upper Miocene interval, recording successive phases of collapse (Silva et al. 1999, 2009; Reis et al. 2010, 2016). Above the upper detachment level, the on-going collapse of the Amazon fan is expressed as paired belts of extensional and compressional faults across the shelf and upper slope above water depths of 2100 m, including thrust-folds with up to 500 m of seafloor relief (Silva et al., 1999, 2009; Reis et al., 2010, 2016).

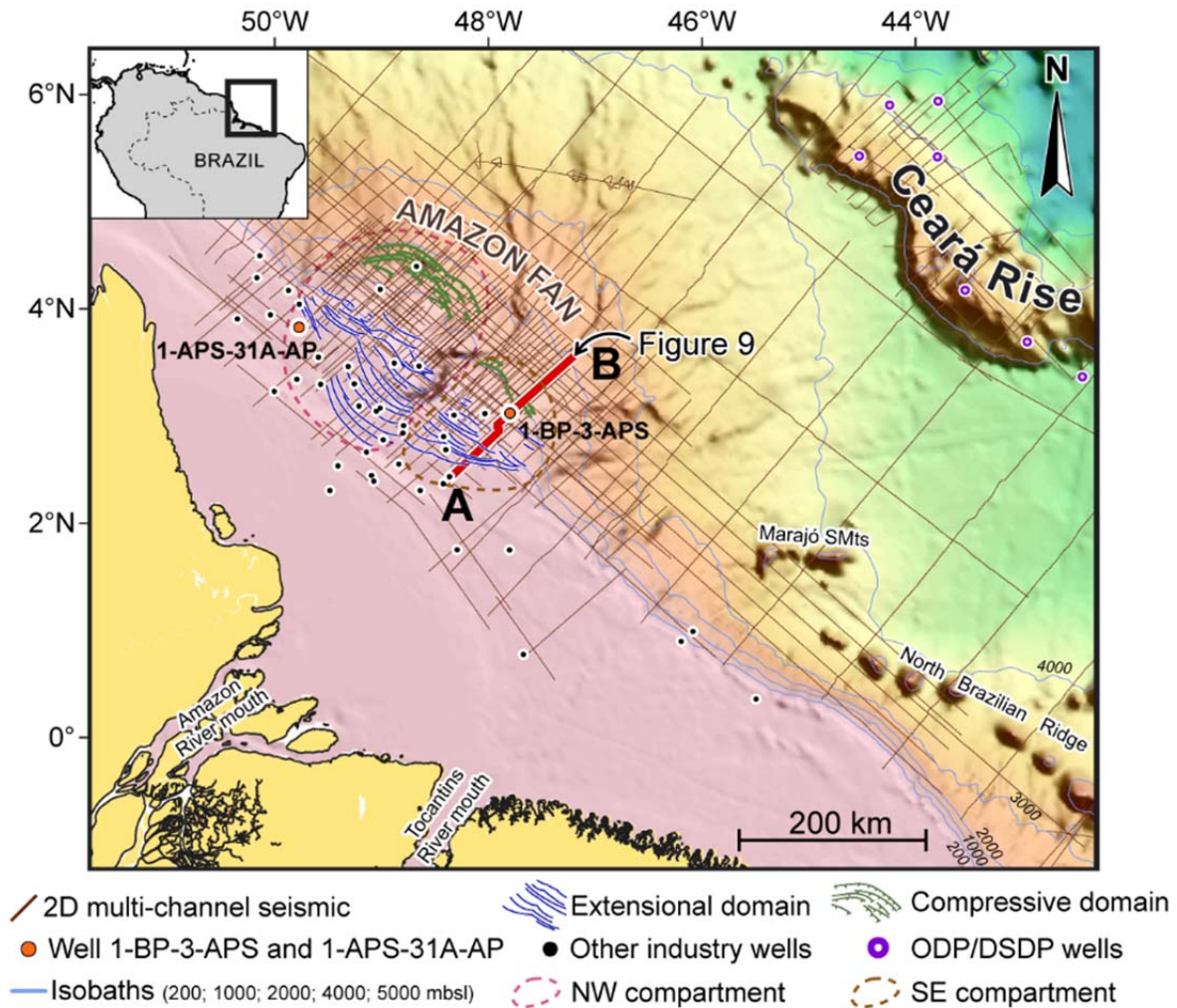


Figure 5.1: Bathymetry of the Equatorial Margin of Brazil showing the location of the Amazon Fan and available seismic profiles and wells. The Amazon Fan is composed of NW and SE structural compartments, as defined by [Cobbold et al \(2004\)](#) and [Oliveira et al \(2005\)](#). Gravitational collapse has resulted in paired domains of extensional and compressive faults across the shelf and upper slope. The available regional dataset comprises multi-channel seismic reflection profiles and drilling results from industry and ODP/DSDP wells. For this study, we use a composite seismic profile across the SW compartment referred to as A-B, shown in red, calibrated with reference to two wells: 1-BP-3-APS and 1-APS-31A-AP (also shown in red).

Detachment surfaces within the Amazon Fan have been inferred to correspond to weak levels composed of overpressured clays (Oliveira, 2005; Zalán and Oliveira, 2005; Perovano et al., 2009, 2011). Based on sandbox modeling, Cobbold et al (2004) proposed that the structural patterns of the Amazon fan could be reproduced on the assumption that fluid overpressures existed over a triangular area beneath the detachment. They noted that deep wells had encountered overpressures within the upper several kilometers of the fan, and suggested that numerical modeling (not presented) supported the origin of the fluids from thermogenic gas generation from Cenomanian-Turonian source rocks beneath the detachment. Evidence for an active hydrocarbon system within the Foz do Amazonas Basin is available from results from published wells reports (Brazilian Petroleum and Gas Agency - ANP) that indicate thermogenic hydrocarbons, mainly gas. Miranda et al (1998) used satellite data to identify natural oil seeps at the sea surface above growth faults and thrust-folds across the shelf break and upper slope, mainly in the Northwest part of the Amazon fan. In the same area, Ketzer et al (2018) presented multibeam sonar evidence of gas flares rising up to 900 m into the water column from seafloor vents in water depths of 650-2600 m, while samples of gas hydrates were recovered at three sites and found to contain methane isotopically consistent with biogenic sources and with possible thermogenic contributions at a site north-western of the fan.

The objective of this paper is to investigate the evolution of pore fluid pressure during growth and gravitational collapse of the Amazon Fan. This is approached through the application of modeling techniques commonly used for petroleum systems, here applied for what we believe to be the first time to a late Cenozoic continental margin depocentre. The study is based on the interpretation of commercial 2D seismic reflection data across the shelf and slope, stratigraphically and geomechanically constrained by well data; these data are used to undertake a 2D kinematic restoration, followed by forward modeling of the evolution of pore pressure and temperature along the section. The results allow us to investigate potential overpressure mechanisms and discuss their implications for the operation of the

detachment surface. Our findings provide new constraints on the relative roles of fluid generation versus compaction in driving gravity tectonics within the Amazon fan, and provide insights applicable to other rapidly deposited continental margin depocentres.

V.2 GEOLOGICAL SETTING

The Foz do Amazonas Basin was formed as a consequence of rifting of the South American and African plates from the Aptian to the Cenomanian. The basin is characterized by multiple phases of subsidence and a complex structural style influenced by transtensional tectonism (Matos, 2000). According to Brandão and Feijó (1994) and Figueiredo et al. (2007), the syn-rift phase of the Foz do Amazonas Basin took place between the Valanginian and the Albian and was marked by the deposition of fluvio-deltaic, lacustrine and marine sediments filling pull-apart half-grabens (Cassiporé and Codó Formations; Fig. 5.2). The post-rift phase saw the widespread deposition of open marine mudstones and siltstones of the Limoeiro Formation between latest Albian and Maastrichtian (from c. 101 to c. 66 Ma; Figueiredo et al., 2007; Boulila et al., 2020). From Paleocene to late Miocene (c. 66 to 8 Ma), shelf sedimentation resulted in a mixed carbonate-siliciclastic platform up to 4000 m thick, laterally equivalent to thinner deep-water calcilutites and mudstones deposits (Marajo, Amapá and Travosas Formations - Wolff and Carozzi, 1984; Gorini et al., 2014; Cruz et al., 2019). The final phase of post-rift deposition took place from c. 8 Ma, and involved a massive influx of siliciclastic sediments that suppressed carbonate production over most of the shelf (Figueiredo et al., 2009; Gorini et al., 2014). This final phase corresponds to the establishment of a trans-continental Amazon River from the late Miocene (Hoorn et al. 2017) and the growth of the Amazon deep-sea fan as a prograding sediment wedge up to 10 km thick beneath the continental shelf and slope (Figueiredo et al., 2009; Cruz et al., 2019).

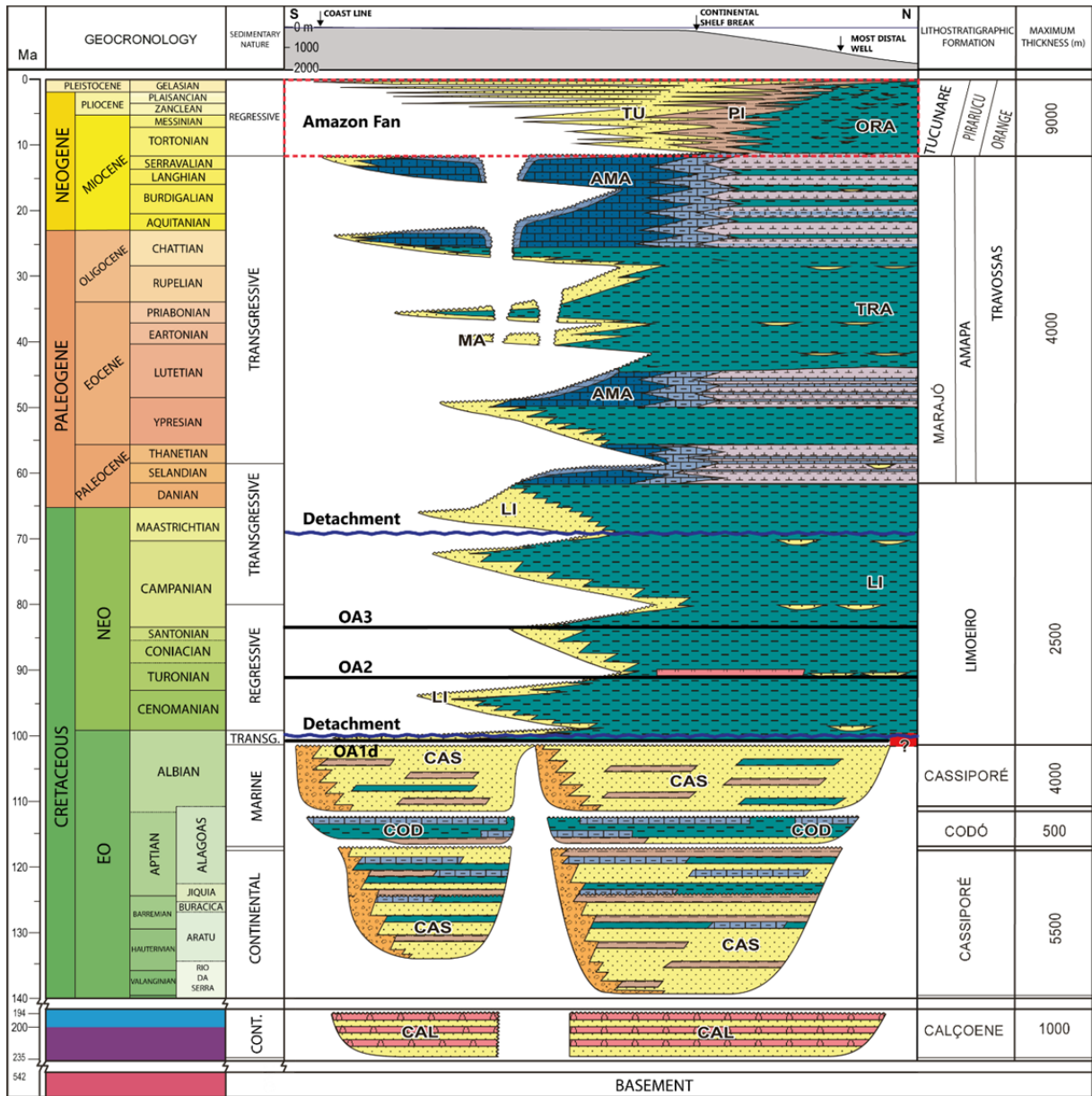


Figure 5.2: Foz do Amazonas Basin stratigraphy chart, focusing on the Amazon Fan. Detachment levels (Albian c. 100Ma and Upper Cretaceous c. 69.7Ma) and likely levels of Oceanic Anoxic Events (OAE1d c. 101.1Ma, OAE2 c. 93.5Ma and OAE3 c. 83.6Ma), representing the potential source rocks have been added. Modified from [Figueiredo et al. \(2007\)](#).

The Upper Miocene to Quaternary succession of the Amazon fan contains allochthonous masses corresponding to stacked megaslide complexes sourced from the upper slope, argued to record triggering by gravity tectonics during three main collapse phases in the Late Miocene-Upper Pliocene, the mid-Pliocene-Pleistocene, and from the mid-Pleistocene (Reis et al., 2016). Collapse of the upper Amazon fan has resulted in paired extensional and compressional belts (Fig. 5.1) that affect the sedimentary sequence from Cretaceous to recent, consisting of listric normal faults across the shelf and upper slope, and reverse faults and fold-and-thrust structures to depths of 2100 m (Silva et al., 1999; Cobbold et al., 2004; Oliveira, 2005; Oliveira et al., 2005; Reis et al., 2010, 2016; Perovano et al., 2011). Three regional detachment surfaces have been identified from seismic interpretation of fault geometries and linked to shale successions (Fig. 5.2) : lower and intermediate detachments at the top of the Albian (c. 100 Ma) and at Upper Cretaceous (c. 69.7 Ma) (Silva et al., 1999; Perovano et al., 2009, 2011) and an upper detachment level within the upper Miocene at the base of the Amazon fan (Silva et al., 2009; Reis et al., 2010, 2016).

The Amazon Fan is characterized by two asymmetric structural compartments, referred to as the Northwest and the Southeast, separated by the Amazon canyon (Fig. 5.1), each associated with thin-skinned extensional and compressional structures rooted on detachment surfaces (Cobbold et al., 2004; Oliveira et al., 2005). The NW compartment is the larger (>200 km in seaward extent) and thicker (up to 10 km), and is structurally more complex, with evidence of long-lasting compressional deformation along multiple overlapping fronts that have caused up to 500 m of seafloor relief (Cobbold et al., 2004; Oliveira et al., 2005) . The SE compartment is smaller (<100 km wide) and the compressional system is restricted to a pair of active reverse faults that cause no major seafloor relief. Our study focuses on the SE compartment of the Amazon Fan deformation related to the base Tertiary detachment surface in the SE compartment.

V.3 DATA AND METHODS

The study is based on exploration data obtained from the Brazilian Petroleum and Gas Agency (ANP), comprising a composite multichannel seismic reflection profile calibrated with data from exploration wells (Fig. 5.1). These data were analyzed following the methodological steps shown in Fig. 5.3 and described below, involving an interpretation and kinematic restoration of the seismic profile, 1D geomechanical modeling to obtain a present-day pore pressure profile, 2D basin modeling of pore pressure and temperature evolution and finally 2D mechanical modeling of pore pressure evolution along the detachment.

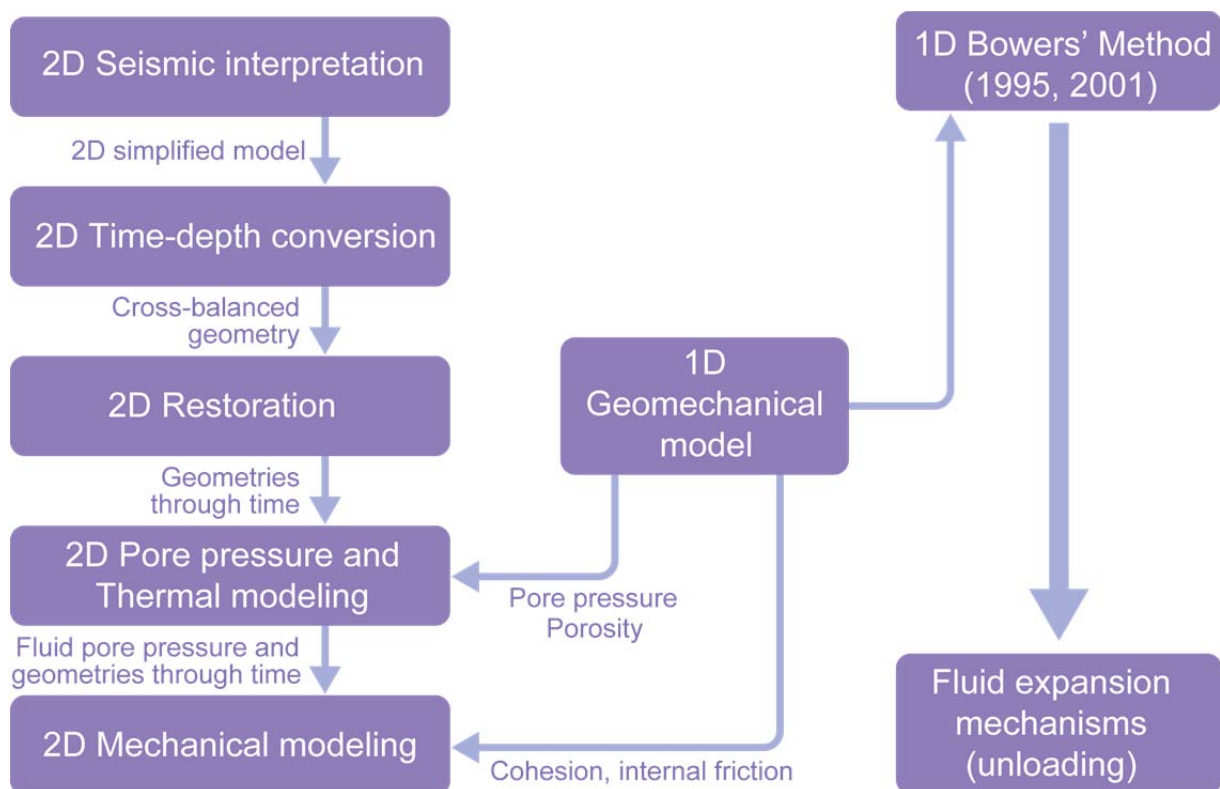


Figure 5.3: Methodology applied to seismic and well data to investigate the evolution of pore fluid pressure in the Amazon Fan.

V.3.1 Well data

The study uses data from 32 industry wells on the continental shelf and upper slope and from Ocean Drilling Program (ODP) site 931 on the middle slope (Fig. 5.1, Table 5.1). From all wells, composite logs, sonic profiles and check shot data were used as input to the interpretation and time-depth conversion of seismic data (Table 5.1; see below). Additional data from two wells, 1-BP-3-APS and 1-APS-31A-AP (Fig. 5.1, Table 5.1), were used as input to geomechanical and basin modeling: density and gamma ray logs were used from both wells, while from 1-BP-3-APS we also used the resistivity and calibration data including direct formation pressure and temperature measurements, leak-off tests (LOTs) and well markers. In addition, porosity data from ODP site 931 (Table 5.1; [Flood et al., 1995](#)) were used as input to 2D basin modeling.

Table 5.1: Well data set available for this paper.

Wells	Water depth (mbsl)	Total depth (mbsl)	Composite log	Sonic	Check shots	Gamma-ray	Density (RhoB)	Others
1-APS-31A-AP	91	4928	✓	✓		✓	✓	mud weight, temperature, LOTs porosities
1BP-3-AP	754	5625	✓	✓		✓	✓	
Site 931	3475	421						
1-APS-01-AP	21	4812.8	✓	✓				
1-APS-04-AP	87	4917	✓	✓				
1-APS-05-AP	88	4354	✓	✓				
1-APS-06A-AP	84.7	4714.6	✓	✓				
1-APS-07-AP	74	4630	✓	✓				
1-APS-11-AP	80	3931	✓	✓				
1-APS-12-AP	91	4407	✓	✓	✓			
1-APS-14-AP	88.6	5000	✓	✓				
1-APS-17-AP	81.4	5092	✓	✓	✓			
1-APS-18-AP	84	3987	✓	✓	✓			
1-APS-20B-AP	144.5	3542	✓	✓				
1-APS-22-AP	107	3704	✓	✓				
1-APS-24-AP	22	4847	✓	✓				
1-APS-25-AP	73	4400	✓	✓	✓			
1-APS-27A-AP	95	2415.5	✓	✓	✓			
1-APS-29-AP	98.7	4592	✓	✓				
1-APS-30-AP	125.6	3736.5	✓	✓	✓			
1-APS-32-AP	96	3969	✓	✓	✓			
1-APS-35-AP	80.7	3998	✓	✓	✓			
1-APS-36-AP	89	4673	✓	✓				
1-APS-41-AP	36	4211	✓	✓				
1-APS-44A-AP	140	4123	✓	✓	✓			
1-APS-45B-AP	104.7	4432	✓	✓	✓			
1-APS-47B-AP	19.8	4485	✓	✓				
1-APS-51A-AP	438	3986	✓	✓				
1-APS-52-AP	103.7	4698.5	✓	✓	✓			
1-APS-53-AP	180	3572	✓	✓	✓			
1-APS-54A-AP	115	3984	✓	✓	✓			
1-BP-2-AP	967	5152	✓	✓				

V.3.2 Composite seismic reflection profile

The profile used for this study crosses the SE structural compartment of the Amazon fan (Fig. 5.1). The 192 km long multichannel seismic profile A-B is a composite of two shorter profiles, each of which have a record length of 12 seconds two-way travel time (TWTT), with vertical resolution of 10–50 m (depending on depth and lithology). The two profiles were subject to standard processing techniques including post-stack time migration (PSTM). The composite profile was interpreted using standard techniques of seismic sequence stratigraphy, and correlation of horizons to regional wells (Fig. 5.1) with reference to the stratigraphic framework detailed by [Cruz \(2018, Cruz et al., 2019\)](#).

V.3.3 Time-depth conversion of interpreted section

The stratigraphic and structural interpretation along section A-B was converted from TWTT to depth using a layer cake method ([Marsden, 1989](#)). The technique takes into account geological layers, bounded by time horizons, and laterally varying interval velocities for each layer ([Etris et al., 2001](#)). For the conversion, we used: 1) gridded maps of horizons picked along the composite profile A-B in TWTT and along other profiles of the regional seismic grid (Fig. 5.1), including the seafloor, 2) well markers to identify the ages of the intervals bound by the horizons (see Table 5.2), 3) for each layer younger than 69.7 Ma, a map of interval velocities from industry wells based on sonic logs and check shots (Fig. 5.1, Table 5.1) and 4) for older/deeper layers, refraction velocities from [Watts et al \(2009\)](#) (Table 5.2).

Table 5.2: Interval velocities attributed to pseudo-wells and to well 1-BP-3-APS as control on the time-depth conversion of section A-B (see Fig. 5.5). Velocities for ages younger than 69.7Ma were based on sonic log and check shots from industry wells; for 69.7–120Ma interval age, velocities were based on [Watts et al. \(2009\)](#).

Interval Velocities (m/s)						
Age Interval	Pseudo-well 1	Pseudo-well 2	Pseudo-well 3	Pseudo-well 4	1-BP-3-APS	Pseudo-well 5
0 - 2	2080	2070	2060	2050	2175	2157
2 - 3,7	2445	2320	2235	2195	2390	2373
3,7 - 5,5	2770	2395	2195	2200	2522	2489
5,5 - 8	3000	2530	2390	2350	2730	2682
8 - 24	3290	2625	2385	2310	2870	2792
24 - 28	3650	2735	2450	2350	3060	2964
28 - 33,5	3775	2795	2470	2405	3170	3058
33,5 - 38	3765	2800	2500	2500	3250	3129
38 - 66	3800	2855	2540	2560	3415	3275
66 - 69,7	4000	3000	2580	2560	3415	2827
69,7 - 83,6	4100	3700	2940	2940	3050	3300
83,6 - 93,5	4100	3700	2940	2940	3050	3300
93,5 - 100	4100	3700	2940	2940	3050	3300
100 - 101,1	4100	3700	2940	2940	3050	3300
101,1 - 102	4100	3700	2940	2940	3050	3300
102 - 120	4100	3700	2940	2940	3050	3300

V.3.4 2D Structural Restoration

The depth-converted profile was restored using *KronosFlow* (version 2019), a software package developed by IFPEN (*Institut Français du Pétrole et Energies Nouvelles*). The structural evolution is reconstructed based on the relation between faults and sediment thicknesses. Different geological scenarios are built step-by-step and used to simulate the evolution of physical properties (in our case, pressure, temperature and hydrocarbon generation) with a robust calculator called Arctem (Callies et al., 2017). Each reconstruction step involves sequential 2D fault displacements associated with material deformation and mechanical decompaction. The best fitting scenario is finally chosen. A coherent mesh through time is built at each step, on which petroleum system modeling is done.

A 2D starting model in *KronosFlow* requires an initial geometry in depth and an absolute age for each horizon. We interpreted seismic section A-B starting from the stratigraphic scheme of Cruz (2018, Cruz et al., 2019), introducing intermediate horizons to improve the resolution of geometry and lithofacies distribution. In particular, we added horizons in the intervals between the present and 2 Ma and between 3.7 Ma and 5.5 Ma as isopach layer ages.

Some hypothetical constraints were imposed on the restoration:

- mass balance from one step to another was applied with a 5% tolerance
- a paleobathymetric profile was imposed for each restoration age
- undeformed surfaces were assumed for the two detachment levels at 100 Ma and 69.7 Ma and for the basement below those levels
- left and right limits were preserved through time

Thus the restoration was strictly constrained to the borders of the study, by the total volume of material, fault displacements, and the amount of deformation.

V.3.5 Pore pressure estimation from 1D geomechanical models

The present-day pore fluid pressure in well 1-BP-3 –APS was estimated using both the method of [Eaton \(1975\)](#) and that of [Bowers \(1995, 2001\)](#) (see Appendix A for method descriptions). For both methods, we used the JewelSuite Geomechanics Software (Baker Hughes). Eaton's method considers that excess of pore pressure results from undercompaction, i.e. trapped pore fluid has been squeezed by the weight of more recently deposited sediments ([Bowers, 1995](#)). The pore pressure calculated by Eaton's method was used as a calibration data for the 2D pressure modeling, presented in section 5.2.1. Bowers' method allows the presence and depth of fluid expansion mechanisms to be captured from reductions of velocity and effective stress. Quantification of unloading requires downhole information (e.g. mineralogy, gas content, caving analyses) that were not available for this study. Nonetheless, it was possible to use the results from well 1-BP-3 –APS to identify the presence of unloading mechanisms (see section 5.3.3).

V.3.6 2D basin modeling of pore pressure and temperature

Basin modeling involves dynamic forward modeling of multiple geological processes in order to evaluate the pore pressure evolution and temperature history of sedimentary basins ([Hantschel & Kauerauf, 2009](#)). We used the TemisFlow Petroleum System Software (IFPen; version 2019), which integrates geological, geochemical and mechanical data. The input data are the geometries and absolute ages of horizons obtained from the 2D restoration performed by KronosFlow, as well as lithologies, paleobathymetries, boundary conditions, and timing of faults.

V.3.7 2D mechanical modeling

We used Optum G2 (2013) to infer the evolution of pore fluid pressure along the detachment. The software relies on limit analysis theory, which is based on the Mohr-Coulomb criterion and the weak formulation of the force equilibrium ([Salençon, 2002](#), [Chandra et al., 1994](#); [Maillot and Leroy, 2006](#)), and allows prediction of the deformation of a structure submitted to a load from the distribution of its frictional properties ([Krabbenhoft,](#)

2017). Hence, if the deformation is known, the approach can be applied to infer effective frictions of faults (Kuncoro et al., 2015; Cubas et al., 2016; Berthelon et al., 2018). The pore fluid pressure is then deduced from the effective frictions. In this study, for each age, we seek the effective friction along the faults and the detachment to reproduce the deformation predicted from the 2D restoration. To do so, we used a safety factor here defined as the ratio between the load necessary to generate a collapse and the gravitational force ($g = 9.8m/s^2$). Collapse is thus predicted when the safety factor is lower than 1.

V.4 MODEL SET-UP AND CALIBRATION FROM WELL DATA

In this section, we address the setting-up and calibration of the models used to analyze section A-B based on information obtained from wells (see Fig. 5.3). This includes the interpretation of the composite seismic profile (Fig. 5.4), the lithofacies distribution (Fig. 5.5) and the conversion to depth (table 5.2, Fig. 5.5), as well as the estimation of 1D pore pressures to build 2D basin and mechanical models (Figs 5.6-5.10). The latter modeling steps were calibrated using data from two wells: 1-BP-3-APS and 1-APS-31A-AP (Fig. 5.1).

V.4.1 2D seismic interpretation (TWTT)

The stratigraphic and structural interpretation of composite seismic profile A-B (Fig. 5.1) is presented in Fig. 5.4. We identify a total of 15 horizons, together with the seafloor horizon defining 16 stratigraphic intervals younger than 120 Ma; the stratigraphic units are offset by extensional and compressional faults that root on two main detachment surfaces (Fig. 5.4). The interpreted succession is simplified to accommodate limitations in well control, seismic data quality and structural complexity (Fig. 5.4).

The chronostratigraphic framework in Fig. 5.4 is based in part on that presented for the Offshore Amazon Basin by [Cruz \(2018; Cruz et al. 2019\)](#), constrained by biostratigraphic data from 40 wells located on the continental shelf, upper fan and Ceara Rise (see Fig. 5.1). The framework includes nine seismic horizons, dated by [Cruz et al \(2019\)](#) to 2Ma, 3.7Ma, 5.5Ma, 8Ma, 24Ma, 28Ma, 33.5Ma, 38Ma and 66 Ma. To extend this framework downward to older horizons observed along section A-B (Fig. 5.4), we used data from [Erbacher et al \(2004\)](#) on the age of Oceanic Anoxic Events (OAEs) in the Demerara Rise, and from [Boulila et al \(2020\)](#) on their correlation to well data in the adjacent Foz do Amazonas Basin. [Erbacher et al \(2004\)](#) used results from IODP Leg 207, which drilled five sites and recovered multiple samples of OAE 2, dated at c. 93.5 Ma, the Cenomanian/Turonian boundary (“Bonarelli Event”) ([Arthur et al., 1990; Thurow et al., 1992; Bralower et al., 1994](#)), and of OAE 3, dated at c. 89-83.6 Ma (Conician-Santonian) ([Friedrich et al, 2012](#)). We applied these ages to results from [Boulila et al \(2020\)](#), who propose cyclostratigraphic correlations between the OAEs and maximum flooding surfaces identified in well data (total organic carbon and gamma-ray profiles) from the Foz do Amazonas Basin. In addition to OAE 2 and 3, we added an OAE representing potential source rock levels at c.101.1 (OEA1d, Fig. 5.2, [Boulila et al., 2020](#)). To finalize our stratigraphic model for section A-B (Figs 5.2, 5.4), we considered the main detachment surface to correspond to the maximum flooding surface at c. 69.7 Ma (MFS 2), and the deeper

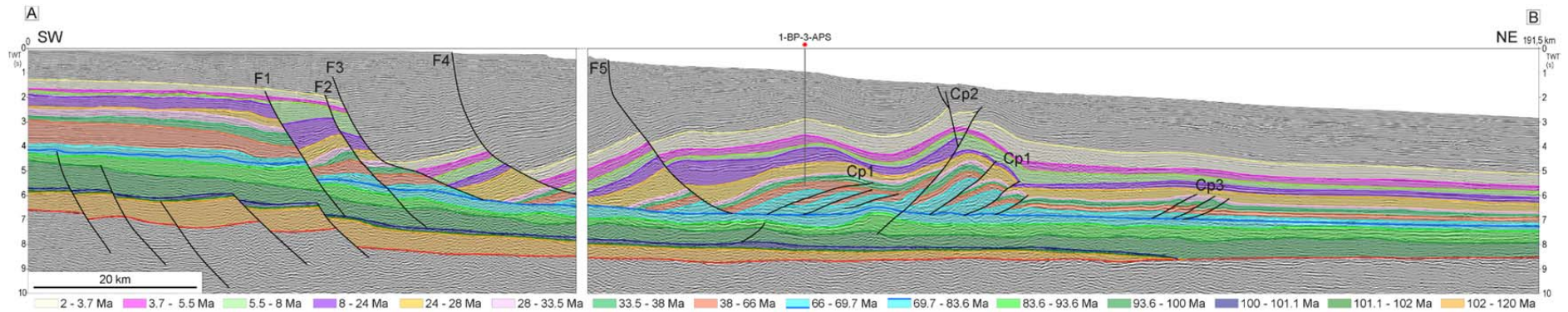


Figure 5.4: Stratigraphic interpretation of the AB seismic profile (inset for location). The succession includes three main intervals: (1) from Lower Aptian to Upper Cretaceous (120 Ma, 102Ma, 101.1Ma, 100Ma, 93.5Ma, 83.6 Ma), delimited on top by a second detachment surface (dark blue horizon, c. 69.7Ma); (2) from Upper Cretaceous to Middle Miocene (66 Ma, 38 Ma, 33.5Ma, 28Ma, 24Ma, 8Ma); (3) from Middle Miocene to present-day (8Ma, 5.5Ma, 3.7Ma, 2Ma and seabed), which corresponds to the Amazon Fan. Gravity tectonics identified along the section are characterized by listric normal faults beneath the shelf and upper slope (F1 to F5) and a compressional domain to seaward (duplexes and thrust faults, Cp1 to Cp3), both rooted on a detachment surface within the Upper Cretaceous (c. 69.7Ma). The slope break is located between F4 and F5.

detachment to correspond to the Upper Albian at c. 100 Ma ([Perovano et al., 2011](#)). We also added the top of the syn-rift succession (Cacipore Formation c. 102 Ma) and a basal horizon at c. 120 Ma ([Brandão & Feijó, 1994](#); [Figueiredo et al., 2007](#)).

The structural interpretation in Fig. 5.4 includes extensional faults across the outer shelf and upper slope and compressional structures to seaward (cf. Fig. 5.1). The main extensional structures are five normal faults (F1 to F5), F1 and F2 rooted on the lower detachment surface and F3-F5 on the upper detachment (dark blue horizon on Fig. 5.4). F4 and F5 reach up to seafloor where they are expressed as scarps. The compressional structures are thrust-folds expressed as duplexes at the detachment front (Cp1 on Fig. 5.4), synthetic and antithetic fault sets (Cp2 on Fig. 5.4) and some buckling to seaward (Cp3 on Fig. 5.4). These structures affect the overlying layers up to the seabed without reaching it, although the seabed is slightly deformed above Cp2 (Fig. 5.4). We note that the seaward extent of compressional features along the profile coincides with that of the lower detachment surface (c. 100Ma, dark blue horizon), which may therefore have played a role in deformation prior to Amazon Fan deposition. Hence, this surface was not taken into account in our study.

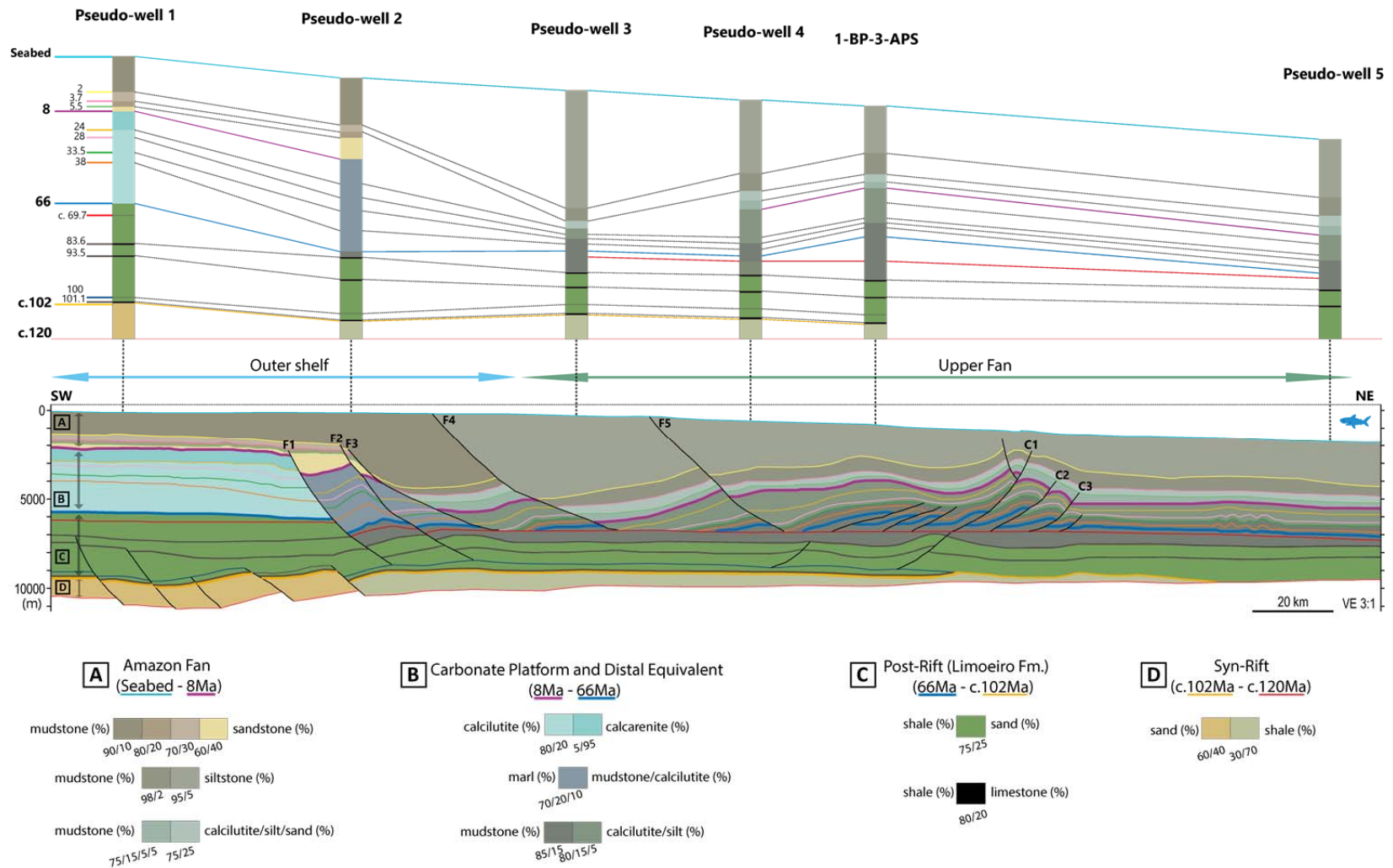


Figure 5.5: Lithofacies model along seismic profile A-B (location in Fig. 5.1), based on information from regional wells and the literature. Also shown are the locations of well 1-BP-3-APS and of pseudo-wells used for the time-depth conversion.

V.4.2 2D lithofacies distribution in depth

Section A-B extends from the outer shelf to the upper fan across water depths of c.75–2150 m. A simplified lithofacies model was created, honoring information regarding the shelf and upper slope domains available from well 1-BP- 3-APS (Fig. 5.1) and from the literature. Three facies groups were created to represent these domains from 66 Ma to present (Fig. 5.5): (1) outer shelf, initially dominated by a carbonate platform later mixed with sandstones and mudstones; (2) transitional domain, dominated by marl, with minor mudstone and carbonate; and (3) upper fan, dominated by mudstones (over 70%), with carbonates and silt fractions (Fig. 5.5).

V.4.3 2D Basin modeling set-up

V.4.3.1 Porosity-permeability relation

The porosity-permeability relation is essential to calibrate 2D pressure modeling. Porosity corresponds to the volume of rock containing fluids. The total porosity includes all space occupied by fluids, including water in clays, which is part of the clay structure and cannot be produced. The total porosity is usually denoted by ϕ_T and defined by:

$$\phi_T = \frac{V_p}{V_t} \quad (\text{Eq. 1})$$

with V_p the volume of the rock occupied by fluids and V_t the total volume of the rock.

Two sets of downhole data were used to build a porosity-depth profile (Fig. 5.6). From seafloor to c. 350 m TVD we used porosity data from ODP site 931, derived from neutron logs and core samples (Flood et al. 1995). From c. 998-5600m TVD we used data from well 1-BP-3-APS, based on petrophysical analysis of acoustic data.

2D pore pressure modeling requires definition of mechanical properties to simulate fluid flow and pore pressure. The Kozeny-Carman equation determines the fluid flow rate that crosses a porous material media, and establishes a relation between porosity and

permeability (Kozeny, 1927; Carman 1937 and 1956). This law is commonly applied to sandstones and carbonates, but may underestimate permeability when applied to shales and mudstones (Chenevert & Sharma, 1991). According to the Kozeny-Carman law, at 3-5 km depth, shales/mudstones with normal compaction are expected to reach 5-9% of porosity for permeabilities of 10^{-4} – 10^{-5} mD. No permeability data are available from the Amazon fan, but at such depths in well 1-BP-3-APS porosities, of 30-40% are observed, consistent with the presence of an undercompacted and overpressured interval. A Kozeny–Carman relation would imply, permeabilities ranging from 10^{-2} - 10^{-3} mD, making it impossible to reproduce present-day pore pressures in the well. Therefore, we established a user-defined porosity-permeability relation for our 2D pressure model, based on the observed porosities and pore pressure of 1-BP-3-APS well (Fig. 5.7). The resulting range of permeability values (10^{-1} - 10^{-7} mD) is consistent with those in the literature for shales, which may reach values of up to 10^{-7} mD (Dickey, 1971; Mesri & Olson, 1971).

Figure 5.7: Porosity-permeability user-defined relation derived from measurements in well 1-BP-3-APS.

V.4.3.2 Boundary conditions

As a first step, we built a crustal model for the study area to extract heat flow at the base of the basin for all ages (Fig. 5.8). To do so, a stretching factor was calculated (McKenzie, 1978), considering (1) a Moho profile inspired by Watts et al., (2009), (2) the top basement surface interpreted from seismic line A-B in depth and (3) an initial crustal thickness of 32 km, divided into upper (20 km) and lower crust (12 km). As a second step, we defined paleobathymetries, based on off-lap breaks observed along the 2D seismic line and literature sources (Brandão & Feijó, 1994; Figueiredo et al., 2007; Cruz, 2018). The third step consisted of defining paleosurface temperatures. For the paleosurface temperature at sea level (0 m), we applied a function derived from paleobathymetry developed by Cardoso and Hamza (2007) and Gutierrez and Hamza (2009). Paleosurface temperatures at depth were based on results from Friedrich et al (2012) and Tremblin et al (2016). Friedrich et al (2012) compiled stable oxygen isotope values of benthic foraminifera sensitive to climatic changes for the period 115-65 Ma, and their relation with paleotemperatures. Tremblin et al (2016) used recent developments in coccolith biogeochemistry to reconstruct equatorial Atlantic sea surface temperature (SST) and atmospheric pCO₂ values from pelagic sequences preceding and spanning the EOT.

Finally, to model 2D hydrocarbon generation, we assumed three potential source rock levels corresponding to Ocean Anoxic Events (Fig. 2): (1) OAE1d, dated c. 101.1Ma, (2) OAE2, dated c. 93.6Ma and (3) OAE3, dated c. 83.6Ma. The kerogen is type II (marine carbonate environment - Mello, 1988; Requejo et al., 1995; Mello et al., 2000). The kinetics was based on PT-beds in Aptian gas-prone source rocks in Brazil (Penteado et al., 2007). The original total organic carbon (TOC) was defined as 8% for all levels based on Erbacher et al (2004), with an average thickness of 50 meters. Residual TOC values range from 1-5%.

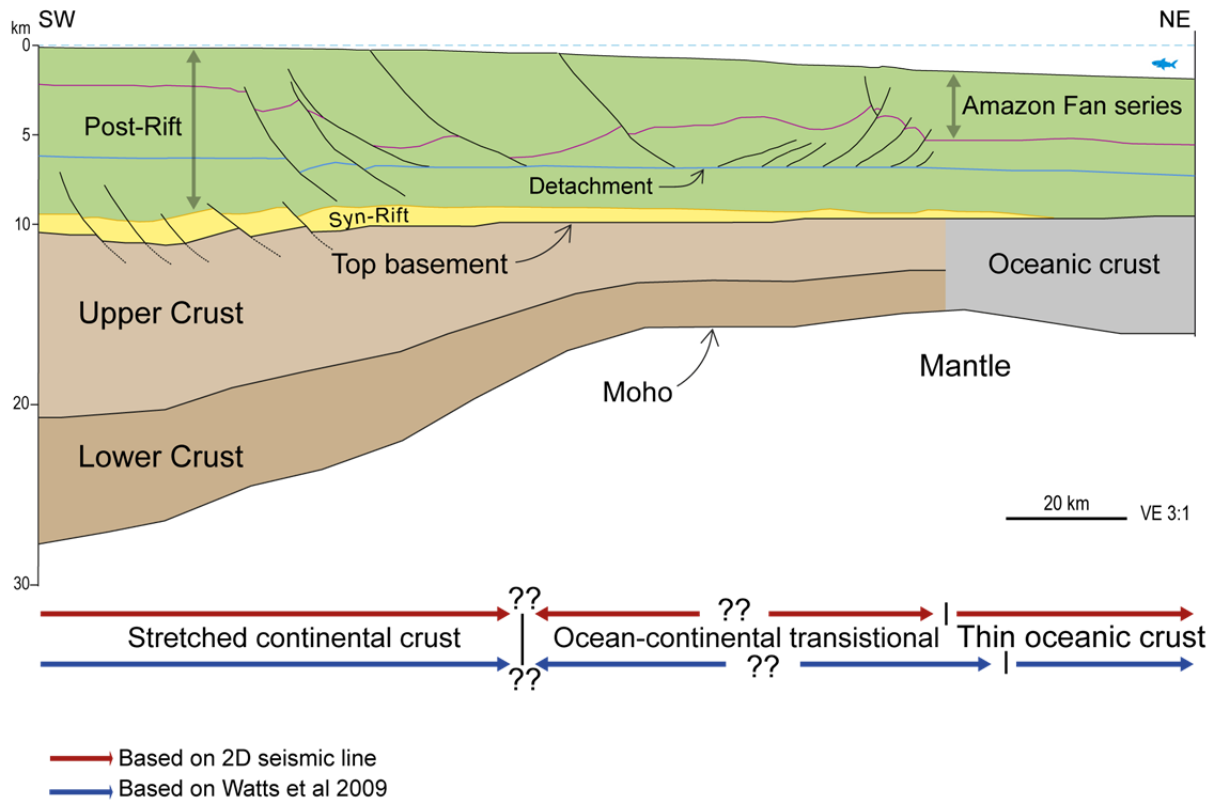


Figure 5.8: Present-day crustal model used to build the thermal scenario. The Moho profile is that identified by [Watts et al \(2009\)](#), shown together with their interpretation of continental to oceanic crustal types (arrows in blue). For our study, we used the top basement and the limit of oceanic crust as interpreted from 2D seismic line (arrows in red).

V.4.4 2D mechanical model set-up

The model requires values of cohesion, friction and pore fluid pressure for each layer. Internal pore fluid pressures were obtained from the 2D basin model. Values for friction and cohesion were deduced from data from wells 1-BP-3-APS and 1-APS-31A-AP. The calculation of internal friction coefficient, cohesion and pore pressure are detailed in Appendix B.

V.5 MODELING RESULTS ALONG PROFILE A-B

In this section, we present the results of the different types of modeling applied to section A-B over the last 8 Ma, i.e. from the onset of Amazon Fan siliciclastic deposition to the present day. The 2D models were performed from 120Ma (base of the model) to the present-day, except for 2D mechanical model which was performed from 8Ma to the present-day. We first present the structural restoration of section A-B, followed by results for the spatial and temporal evolution of temperature and pore pressure within the basin, and their respective implications for fluid and gas generation and fault movements.

V.5.1 2D restoration of SE Amazon Fan growth and deformation

The 2D restoration of the Amazon fan sequential record obtained using KronosFlow are presented in Figure 5.9. Extensional activity (faults F1 and F2, shown in red) and basinward propagation of compressional deformation both start at 8 Ma and persist until 5.5 Ma (Fig. 5.9). During this phase, siliciclastic sedimentation predominates on the shelf (Cruz et al., 2019). From 5.5 Ma to 3.7 Ma, no deformation takes place (Fig. 5.9). During this phase, sediment supply to the SE compartment decreases in favor of the NW one, resulting in the progressive burial of carbonates on the inner NW shelf (Cruz et al., 2019).

Deformation resumes at 2 Ma (F3 and compressive faults C, shown in red on Fig. 5.9), and intensifies from 1.6-1.2 Ma (F3, F4 and C, shown in red). During this phase, F1 and F2 are no longer active. A sequential forward propagation of the extensional domain is observed, at 1.6-1.2 Ma (F3, F4, shown in red), 0.8 Ma (F4, shown in red) and at 0.4 Ma (F4 and F5, shown in red). The compressive domain is also active from 2 Ma, with subsurface fold propagation faults deforming layers up to seafloor (Fig. 5.9). From 0.4 Ma to present, a deep duplex forms at the buried front of the compressive domain, breaking overlying sediments; during the same period, older compressive structures are squeezed and become narrower (Fig. 5.9). However, these faults are not observed to propagate toward the surface.

At the present-day, only normal faults reach the seafloor where they are expressed as scarps (F4 and F5, shown in red on Fig. 5.9).

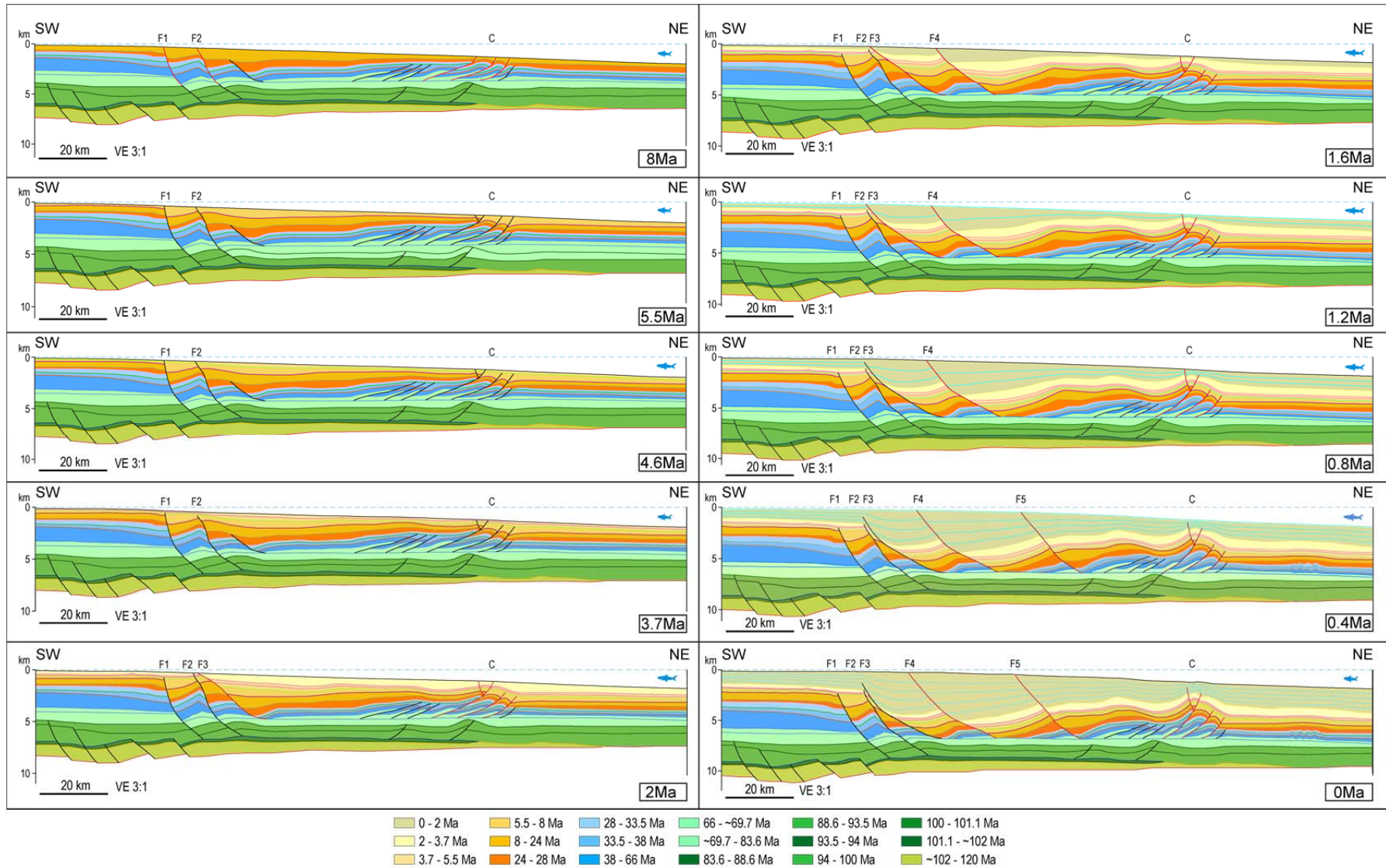


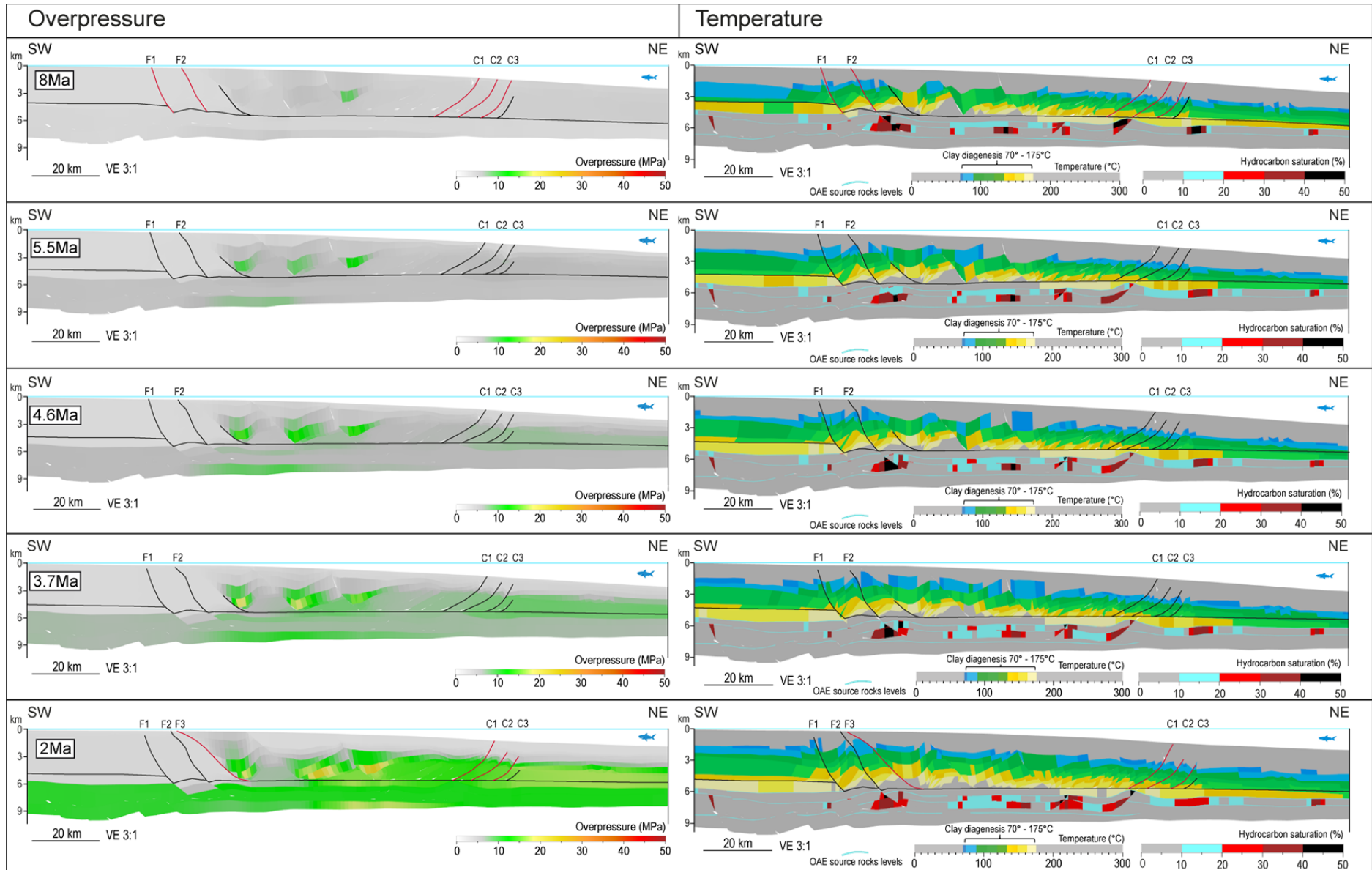
Figure 5.9: 2D restoration along section A-B from 8 Ma to the present day (output from KronosFlow). Active faults are shown in red, inactive in black.

V.5.2 2D basin modeling of pressure and temperature evolution

The results of modeling pore pressure and temperature evolution along section A-B over the last 8 Ma are shown together in Fig. 5.10.

The pore pressure evolution is shown on the left of Fig. 5.10 (active faults are shown in red). At 8 Ma, we do not observe significant overpressure, with most values lower than 10 MPa. Normal faults F1 and F2 and the compressive domain are active (Fig. 5.10). Overpressure increases from 5.5 Ma to 3.7 Ma, but no deformation is observed. Sedimentation rates increase in the fan from 2 Ma, and overpressure increases to 10-20 MPa (Fig. 5.10). From 1.6 Ma to 0.8 Ma, overpressure propagates within the sediment column and along the detachment, increasing significantly (10–40 MPa) between faults F3 and F4 (Fig. 5.10) and near the detachment. Faults F3 and F4 and the compressive domain are active (shown in red in Fig. 5.10). From 0.4 Ma to the present-day, overpressure is well-developed from the extensional domain to the front of the section, and is seen to be compartmentalized by active faults and along the detachment.

The results obtained from 2D thermal modeling are shown on the right of Fig. 5.10, calibrated in terms of two temperature-dependent processes that represent potential mechanisms for overpressure generation (see next section). The smectite-to-illite temperature window is seen to remain above the detachment throughout the simulation (Fig. 5.10). Also shown is the total quantity of oil and gas accumulated over time (hydrocarbon saturation) following migration from three OAE source rocks (see Fig. 5.2), which is seen to be trapped along thickness against faults located below the detachment (Fig. 5.10). These results depend on the modeled thermal history of the area, which is not well-constrained. However, a comparison between bottom hole temperatures measured in well 1-BP-3-APS at around 5.5 km depth and a 1D output from the 2D temperature simulation for the present-day yields a reasonable fit (Fig. 5.11b), suggesting a good calibration.



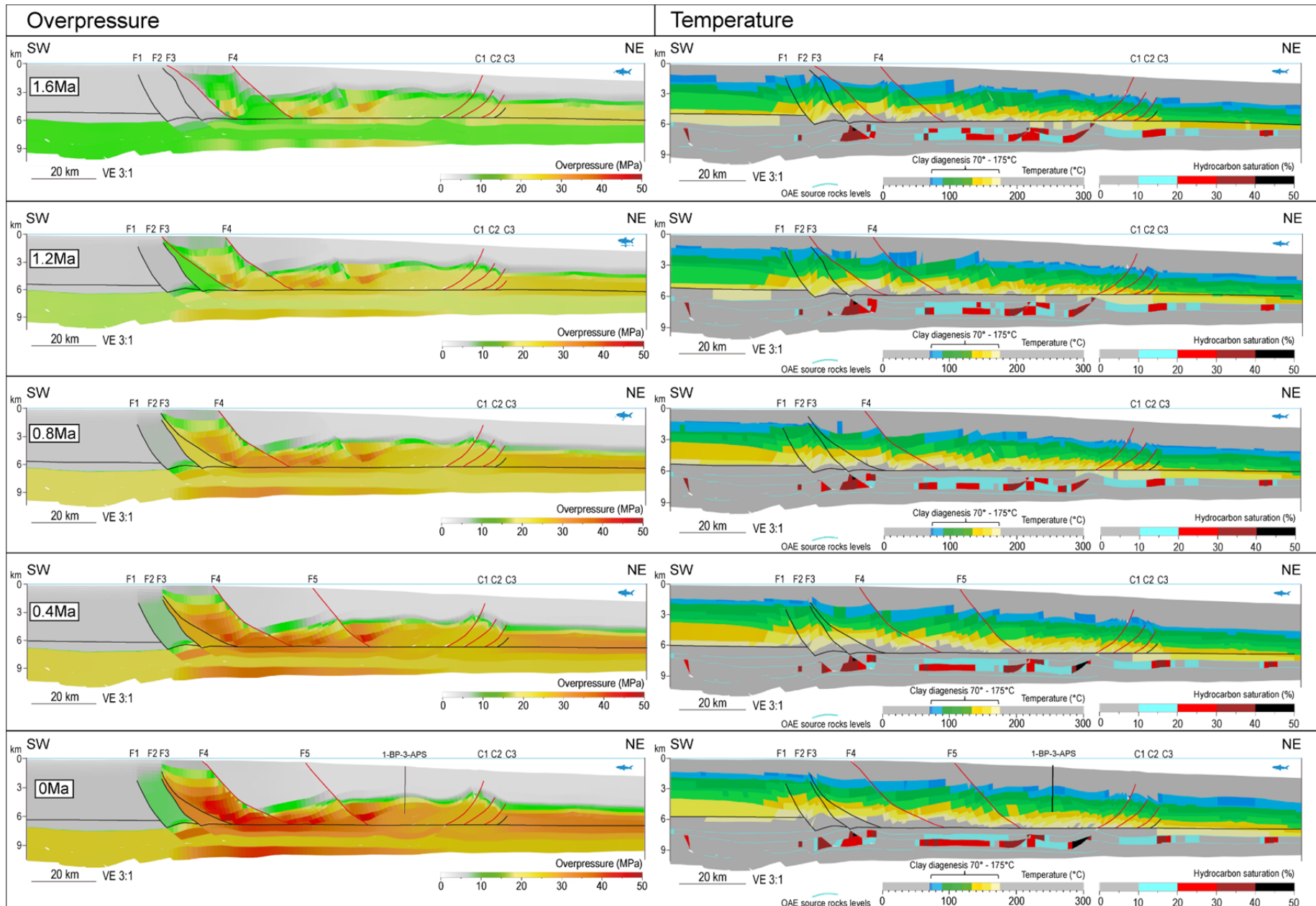


Figure 5.10: Results of modeling pore pressure and temperature

the evolution along section A-B from 8 Ma to the present-day (outputs from TemisFlow). At left: Active faults are shown in red, inactive in black. Overpressure tends to compartmentalize between faults, notably since 2 Ma when sedimentation rates in the Amazon Fan intensified. At right: Temperature results are calibrated in terms of the clay diagenesis window (70-175°C), which remained above the detachment surface from 8 Ma to the present-day. The three OAE source rock levels are efficient over time, reaching the gas expulsion window until 24 Ma (see Fig. 5.14). The total quantity of hydrocarbon (oil and gas) generated was trapped on thickness against faults, where the gas fraction might act as an overpressure generating mechanism.

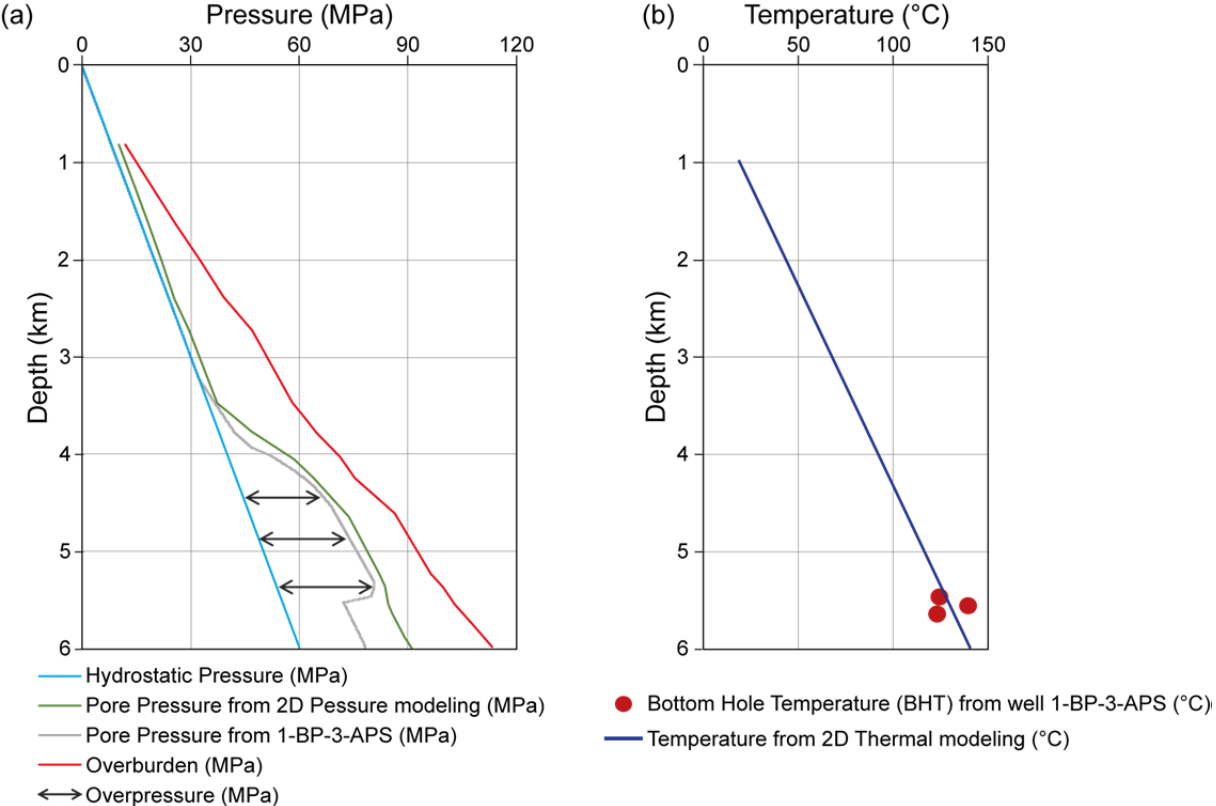


Figure 5.11: Comparison of present-day pore pressures and temperatures in well 1-BP-3-APS with 1D outputs from the 2D model simulations: (a) pressure profile calculated for well 1-BP-3-APS (in grey) using the method of Eaton (1975) compared with 2D model output at the same site (in green); (b) temperatures measured in well 1-BP-3APS compared with 2D model output.

V.5.2.1 Present-day pore pressure

Pore pressures in well 1-BP-3-APS calculated using Eaton's method are hydrostatic down to 3.2km depth, followed by a pore pressure ramp significantly increasing at 3.8 km depth (Fig. 5.12). The maximum pore pressure reaches 82 MPa at approximately 5.3 km depth (c. 38 Ma).

To calibrate our model, we extracted a 1D pore pressure profile at the same position of 1-BP-3-APS well from the 2D pressure modeling at the present-day and compared it with the results from Eaton's method (Fig. 5.11a). The two profiles are comparable, with a pore overpressure ramp from 3.2 to 5.5 km depth.

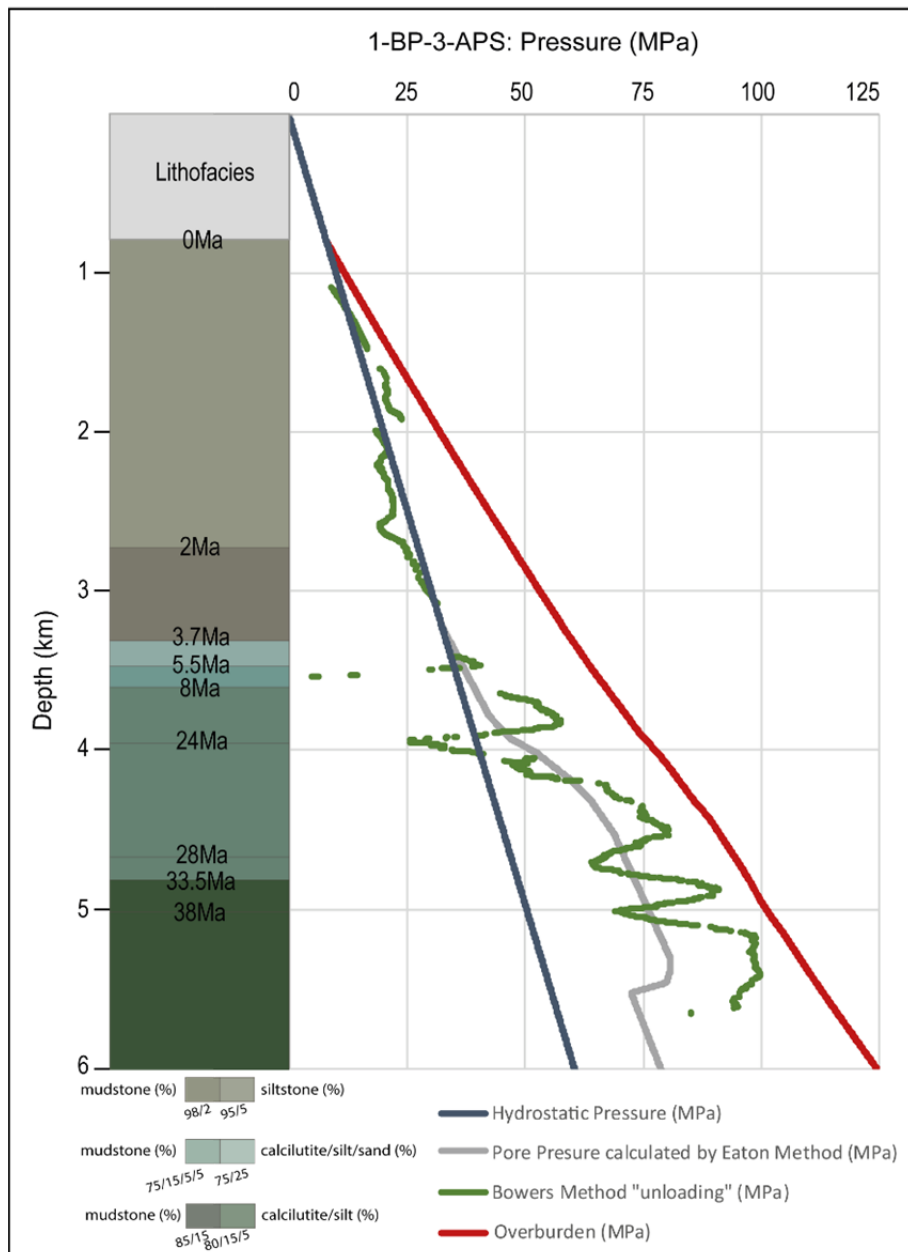


Figure 5.12: Pressure-depth plots for well 1-BP-3-APS well obtained using the methods of [Bowers \(1995, 2001\)](#) and [Eaton \(1975\)](#). The two methods result in comparable trends of pore pressure and indicate the existence of present-day fluid expansion mechanisms from at least 3200-5500 m.

V.5.3 Temperature-driven fluid expansion mechanisms

Results from the 2D temperature modeling were used to analyze two temperature-dependent processes that represent potential overpressure mechanisms, smectite-illite transition and hydrocarbon gas generation. The predicted distribution of fluid expansion mechanisms are checked against present-day pore pressure conditions in well 1-BP-3-APS using Bowers' method.

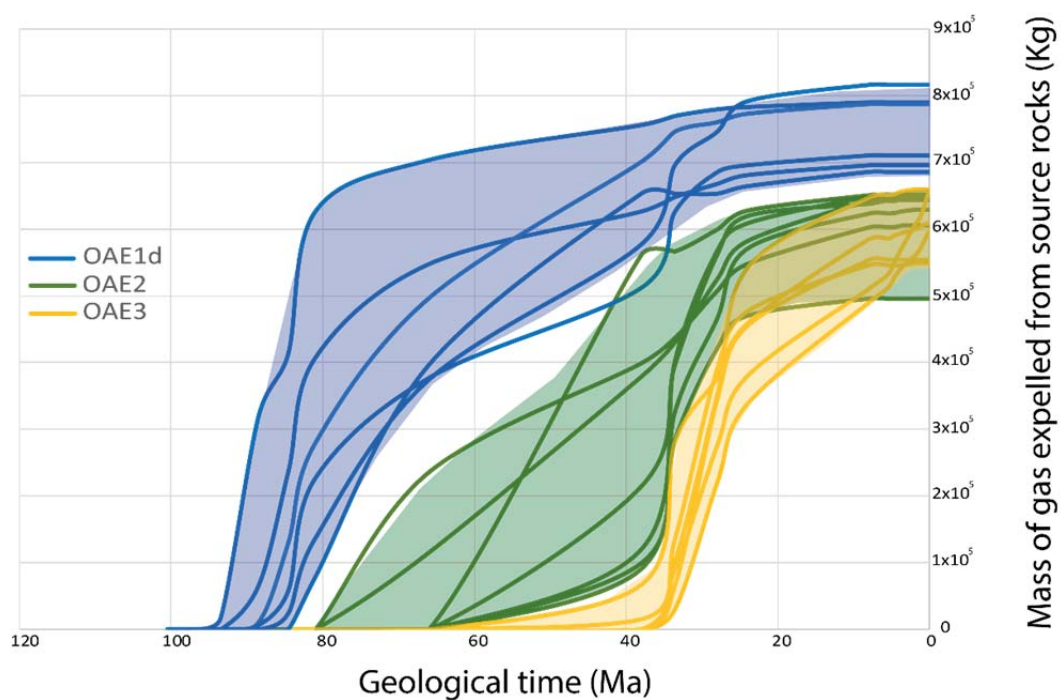
V.5.3.1 Clay mineral transformation

The diagenesis of clay minerals during lithification or post-depositional compaction of sediments may generate overpressure due to the release of bound water, notably during the smectite-illite transition. In mud-dominated basins, a gradual and systematic change from smectite to illite is commonly observed with increasing depth. Bruce (1984) observed a correspondence with high values of overpressure. Hower et al (1976) proposed that the smectite-to-illite transition occurs over a temperature range of 100-175°C, whereas Bruce (1984) gave a range of 70-150°.

The temperature range of 70-175°C modelled along section A-B over the last 8 Ma is shown in Fig.10. Most of the section is dominated by mudstones, including the detachment level and the overlying sedimentary succession. The modelled temperature history clearly supports smectite-illite transition within the Amazon Fan throughout its growth and at the present-day (Fig. 5.10). However, the window of pore water generation resulting from this clay mineral transformation is found to have mainly remained above the detachment surface from 8 Ma to the present-day (Fig. 5.10).

V.5.3.2 Hydrocarbon gas generation

The modeling results along section A-B indicate that the three OAE source rock levels used as input are efficient in terms of the total amount of hydrocarbons expelled (Fig. 5.10). Figure 5.13 presents an average plot of the mass of gas expelled from the source rocks. The expelled gas window for OAE1d lies between c. 100-80 Ma and 33.5 Ma, for OAE2 between c. 80-66 Ma and 24 Ma, and for OAE3 between c. 66 Ma and 24 Ma (Fig. 5.13). We find that almost all gas generated from the three OAE source rock levels was expelled long before the



ons
et of
dep
ositi
on
of
the
Ama
zon
Fan
at
arou

nd 8 Ma.

Figure 5.13: Mass of gas expelled over the last 100 Ma from OAE1d (in blue), OAE2 (in green) and OAE3 (in yellow) source rocks levels (see Fig. 5.2). The curves were extracted at locations along section A-B for each OAE source rock, and grouped to obtain a gas expulsion range. Almost all gas generated was expelled before the onset of deposition of the Amazon Fan around 8 Ma ago.

Fig. 5.10 shows that the hydrocarbons generated migrated preferably along faults to be trapped in older successions at depths of hundreds of meters to a few kilometers beneath the detachment below the detachment. The fraction of gas that migrated and accumulated in these locations, including any gas generated by secondary cracking, represents a potential overpressure generating mechanism. However, from 8 Ma to the present-day, there is no evidence of hydrocarbon migration upward to or along the detachment (Fig. 5.10). Instead, the sequence beneath the detachment (*decollement*) has acted as a natural barrier (or seal) to upward fluid flow. Hydrocarbons are able to migrate upward through successions beneath the detachment (up-dip migration) but would only be able to migrate into overlying successions if there are structures that breach the detachment.

V.5.3.3 Present-day fluid expansion (unloading)

Present-day pore pressures in well 1-BP-3-APS calculated using Eaton's and Bower's methods are compared in Figure 5.12. Both methods show a similar behavior at shallow depth and a ramp at 3.2 km depth. However, at greater depths, Bower's method yields higher pore pressures, reaching 100 MPa at the base of the well. This is because the method of [Bowers \(1995, 2001\)](#) considers unloading as a secondary pressure mechanism. The method considers that an elastic deformation of rocks under high pore pressure is a reversible process and can be identified in the cross-plot of density versus compressional velocity (Fig. 5.14). The plot shows elastic reloading (trend line in violet) when the velocity

drops from 3300 m/s to 1800 m/s without comparable changes in bulk density (c. 2.6 g/cm³), at 3.2-5.5km depth. The results thus provide evidence of unloading in this depth range, consistent with a fluid expansion mechanism.

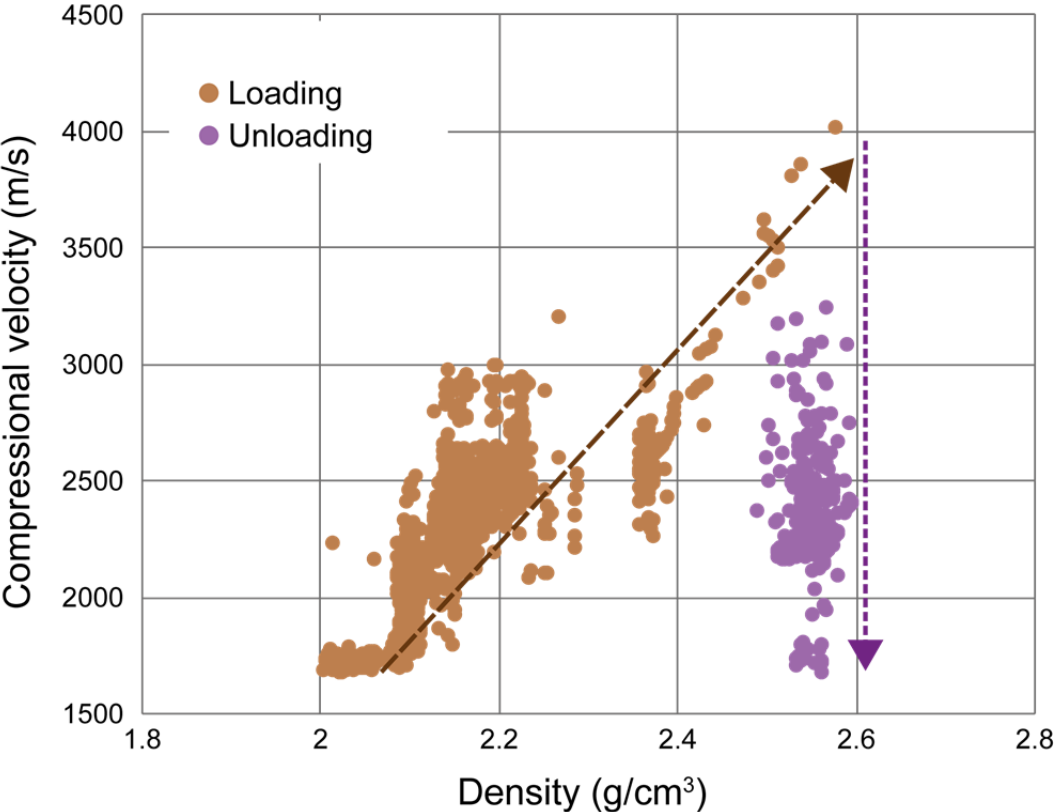


Figure 5.14: Cross-plot of density vs compressional velocity for well 1-BP3-APS, applied to shale/mudstones compaction/unloading behavior. Loading is identified when velocity and density increase proportionally (tendency line in brown), and unloading when velocity decreases and density remains constant (tendency line in violet).

V.5.4 Evolution of deformation along the detachment and faults

To constrain the pore pressure evolution along the detachment and faults in section A-B, we used the OptumG2 software to run a series of trial and error tests, and selected the effective friction along the detachment that best reproduced the observed deformation. When deformation was observed, we searched for the properties producing a factor of safety lower than 1. When no deformation was observed, we checked that the predicted parameters led to a factor of safety larger than 1.

The effective frictions were then converted in pore pressure ratio (λ) assuming a fixed friction for the faults and detachment of 0.4, typical of clays ([Saffer & Marone, 2003](#)). We checked the effect of frictional uncertainties for the sedimentary layers. Slightly different frictions or cohesions led to slightly different pore pressure ratios, with very limited impact on the safety factor, and without producing any significant change on the general trend of the pore pressure evolution.

The results from 8 Ma to present are synthesized in Fig. 5.15, while the vertical and horizontal movements for each model step are given in Figs 5.16 and 5.17.

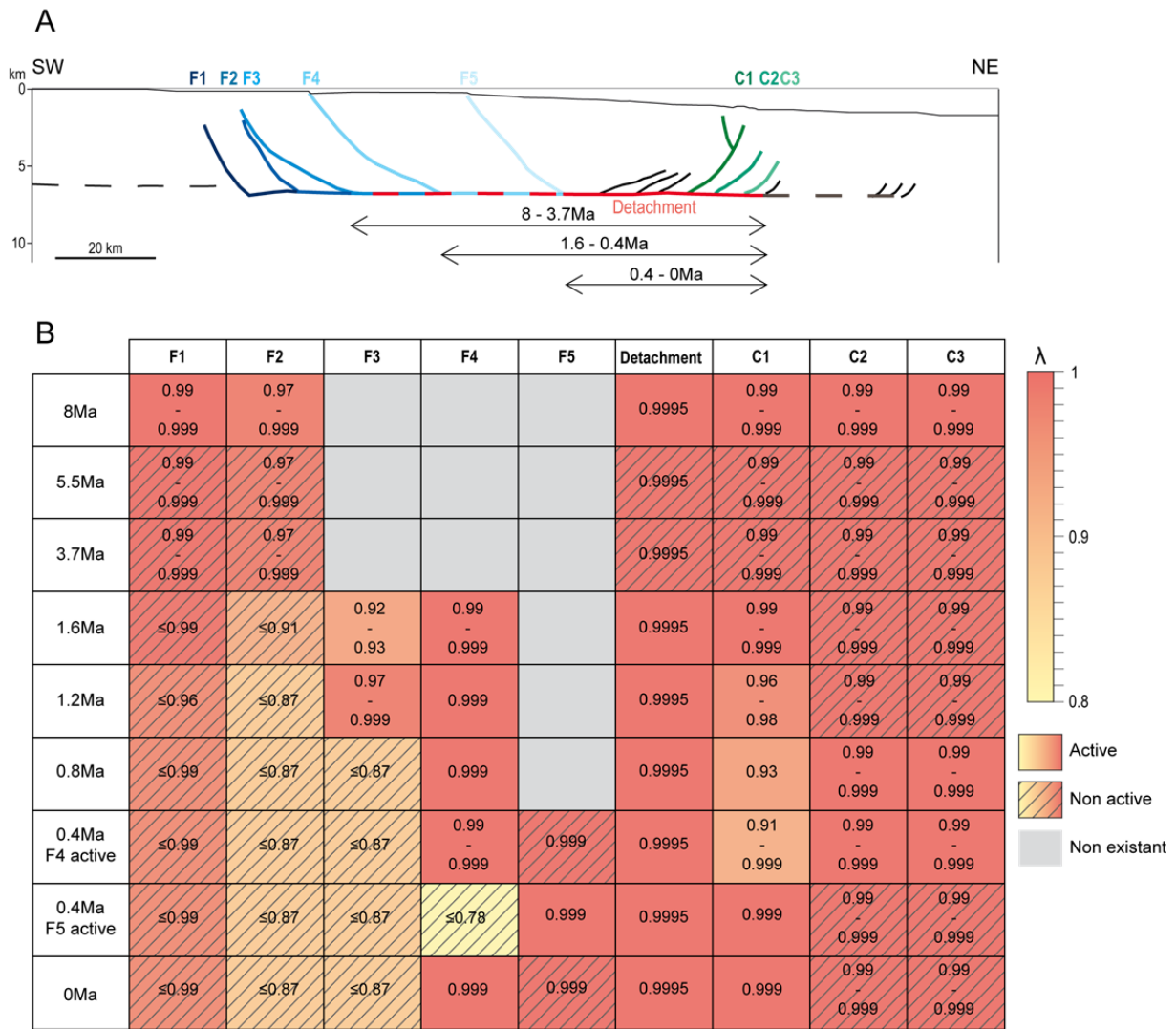


Figure 5.15: Synthesis of deformation over the last 8 Ma along section A-B obtained from mechanical modeling using OptumG2 (A) and the associated evolution of the ratio of fluid pore pressure (λ) along the indicated faults and the detachment (B). To calculate λ , we fixed the friction of faults and detachment to a standard value for clay ($\lambda = 0.4$, Di Toro et al., 2011).

At 8 Ma, lithostatic pore pressure is required along the detachment and all faults in order to generate extension across F1 and F2 and compression along C1, C2 and C3 (Figs 5.15 and 5.16). From 5.5-3.7 Ma, deformation is not possible, even considering a lithostatic pore pressure along the detachment and faults (Fig. 5.16). A stable structure during this period is consistent with our seismic interpretation and restoration, which shows no evidence of deformation. At 1.6 Ma, deformation resumes. In order to lock F1 and F2, a decrease of pore fluid pressure is required. In order to activate F3 and F4, the faults need to reach

lithostatic pore pressure, with higher values along F4 than F3. Therefore, a migration of pore fluid pressure is required, from F1-F2 to F3, and then to F4 is (Figs 5.15 and 5.16). The same scenario holds at 1.2 Ma. At 1.6 and 1.2 Ma, we could not find properties allowing for the activation of C2 and C3 (Figs 5.15 and 5.16). At 0.8 Ma, to abandon F3, a decrease of its pore fluid pressure is necessary, as for F1 and F2 (Figs 5.15 and 5.16). To propagate deformation from C1 to C2-C3, we need to decrease the pore fluid pressure along C1, and increase the pore fluid pressure upward along C2 and C3.

On seismic profile A-B, faults F4 and F5 reach the seabed and form stepped scarps, attesting that the faults are or have recently been active. The compressional domain is also active, since overlying layers are deformed up to the seafloor. However, we could not find a set of properties allowing for the coeval activation of F4 and F5, neither at 0.4 Ma nor at the present-day (Fig. 5.16). We thus considered two alternatives, assuming that deformation may have jumped from F4 to F5 during the last 0.4 Ma (Figs 5.15 and 5.17). To activate F4, the pore fluid pressure along the fault needs to reach lithostatic values. The same applies for F5, however its activation requires a strong decrease of pore fluid pressure along F4. In both cases, a lithostatic pore fluid pressure along C1, C2 and C3 led only to the activation of C1.

To summarize, we are able to reproduce the deformation required by the structural restoration. To do so, a lithostatic pore pressure along the detachment is required at all ages. Moreover, to simulate the migration of the fault activity from F1 to F5, a migration of the pore fluid pressure is required.

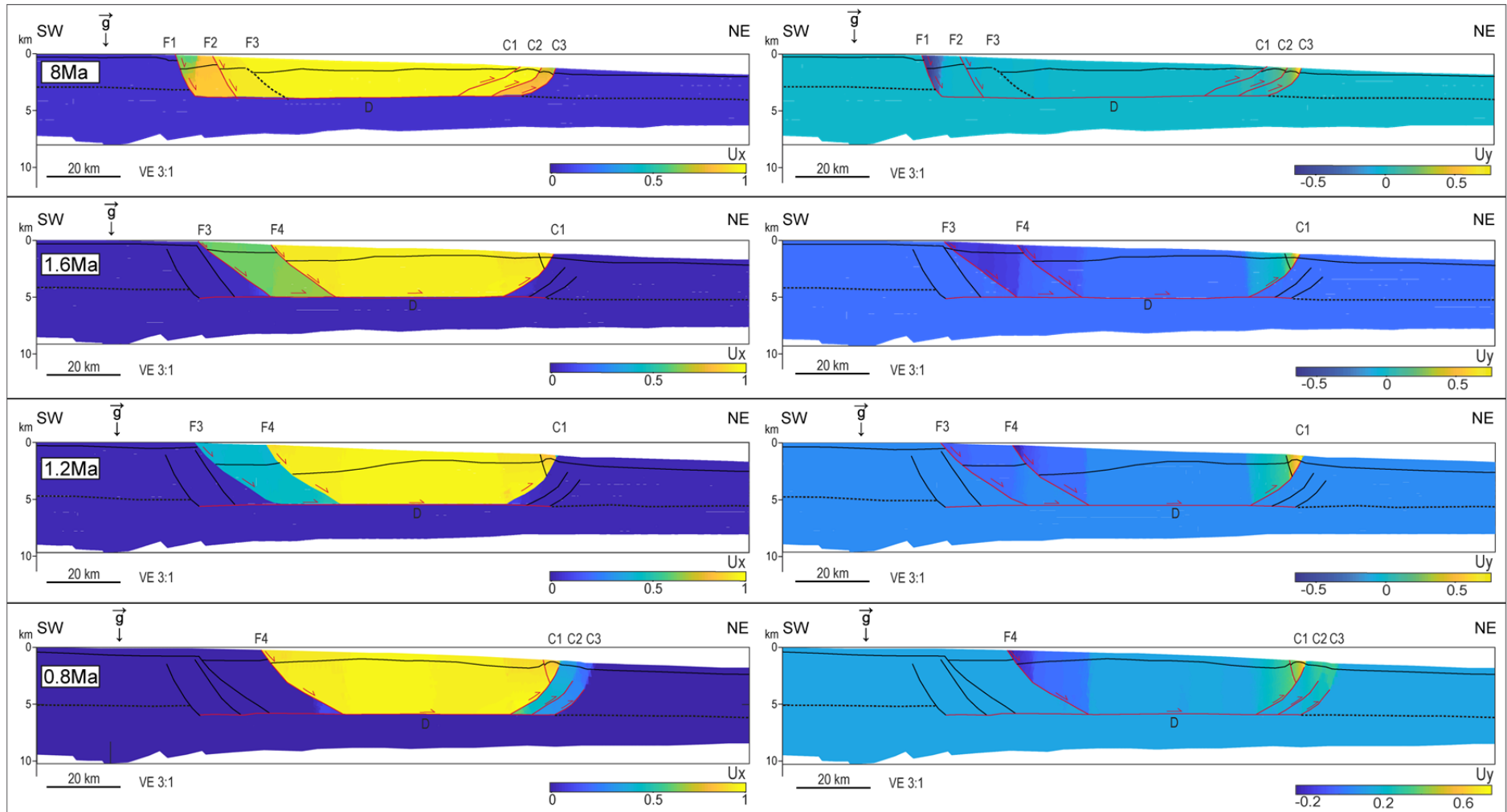


Figure 5.16: 2D Normalized virtual velocities in horizontal and vertical directions obtained from OptumG2, from 8 Ma to 0.8 Ma: (1) 8 Ma, F1 and F2 are active and propagate up to C1, C2 and C3. For the simulation here shown $g = 0.94$. (2) 1.6 Ma, F3 and F4 are active and propagate up to C1 ($g = 0.98$). (3) 1.2 Ma, F3 and F4 are active and propagate only C1 ($g = 0.86$). (4) 0.8 Ma, F4 active and propagate up to C1, C2 and C3 ($g = 0.94$).

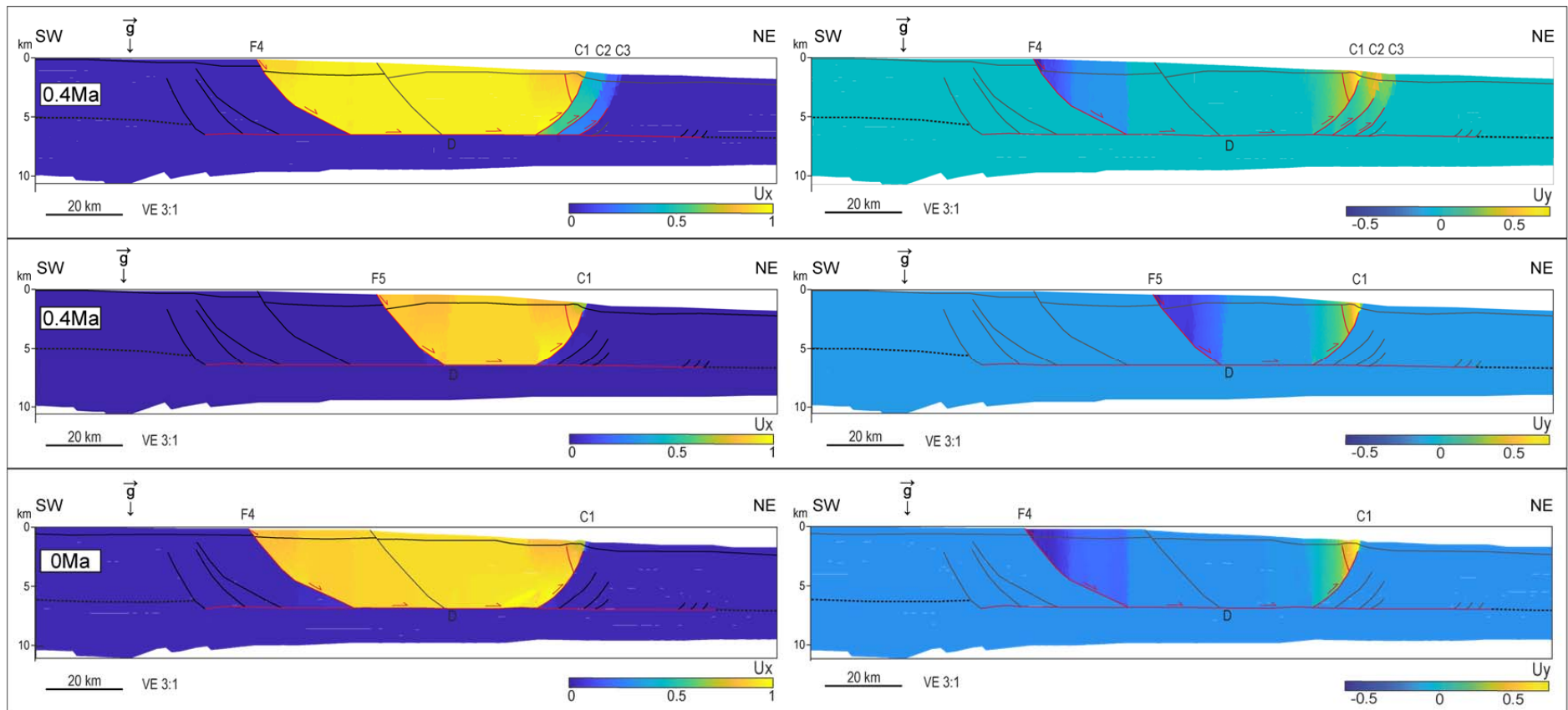
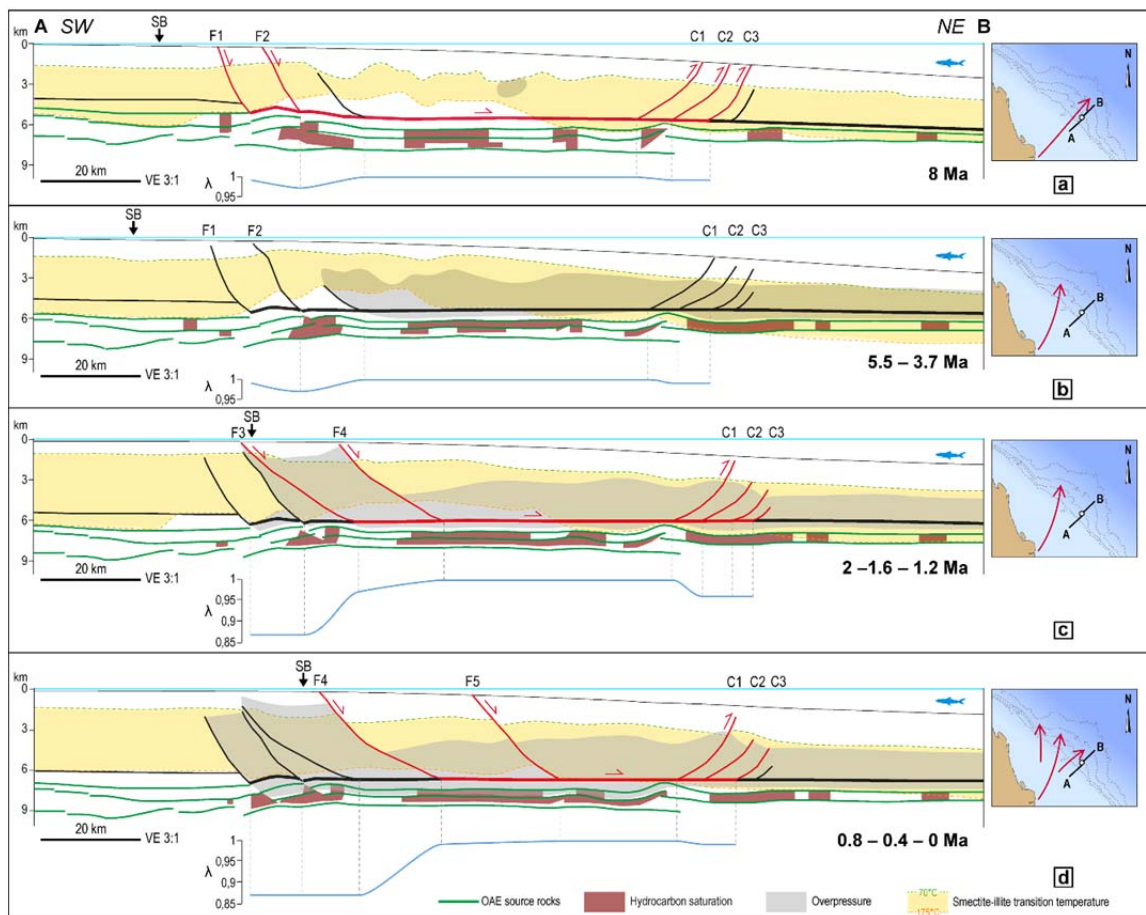


Figure 5.17: 2D Normalized virtual velocities in horizontal and vertical directions obtained from OptumG2, from 0.4 Ma to 0 Ma. Two alternatives are considered at 0.4 Ma: (1) F4 active and propagation to C1, C2 and C3 ($g = 0.95$); (2) F5 active with propagation to C1 ($g = 0.96$); (3) 0 Ma, F4 and C1 active ($g = 0.89$).

V.6. DISCUSSION

The results presented above provide information on the evolution of pressure and temperature within the SE compartment of the Amazon Fan during the accumulation and deformation of up to 6 km of sediment over the last 8 Ma, and their consequences for fluid generation and sediment deformation. The results are synthesized in Fig. 5.18 as four main stages, in order to discuss the controls on the growth and gravitational collapse of this



passive margin depocentre.

Figure 5.18: Synthesis of modeling results along section A-B, grouped into four main stages: (a) 8 Ma, (b) from 5.5 - 3.7Ma, (c) from 2-1.2Ma and (d) from 0.8 to the present-day. Colors indicate the distribution of source rocks and the migration and entrapment of hydrocarbons generated from them beneath the fan, and the distribution of overpressure and the bounds of the smectite-to-illite transition window within the fan. Detachment and fault activities related to gravitational deformation are indicated at each stage (active red, inactive in black) over time, associated evolution of the ratio of fluid pore

pressure (λ , graph in blue). The seaward migration of the shelf break (SB) is indicated, and the inset maps at right indicate the changing directions of sediment supply to the Amazon Fan.

V.6.1 Pore pressure evolution in the southeast Amazon Fan

At 8 Ma, the onset of Amazon fan growth was marked by an increased influx of siliciclastic sediments (Fig. 18a). In response, the SE compartment of the Amazon fan underwent a phase of gravitational collapse, leading to the activation of two listric normal faults (F1, F2) and generating compression at the thrust front. This deformation was generated by stress field variation, caused both by the rapid deposition of sediments and by changes in effective stress due to increasing pore pressures along the detachment. Our basin modeling results indicate that overpressure starts to increase through time (Fig. 5.12, 5.18). Modelled temperatures indicate that the lower part of the smectite-illite transition window intersected the detachment below the continental shelf (landward of F1) and to seaward beneath the compressional domain (Fig. 5.18a), and so could have contributed to increased overpressure in these areas. The modeling results further indicate that the three OAE source rock levels identified beneath the central part of the fan reached maturity by 8 Ma and almost generated thermogenic gas were expelled and migrated over basin (Fig. 5.14). Gas trapped in successions at depths of hundreds to a few thousand meters beneath the detachment might account for overpressure at these depths, but the values are not significant ($< 5\text{MPa}$). At this stage of fan growth, the slope break is located landward of the first active normal fault F1.

From 5.5-3.7 Ma (Fig. 5.18b), sediment supply from the Amazon River was deviated to the larger NW compartment, as testified by progressive burial of the Amapá carbonates on the shelf (Cruz et al., 2019). Decreased sediment supply to the SE compartment can account for the lack of deformation observed along section A-B, consistent with the results of 2D mechanical modeling (Figs 5.15, 5.16). Even considering a high pore pressure along the detachment, collapse structures within the Amazon fan are inactive at this stage. Nonetheless, overpressure continues to build within the fan (grey on Fig. 5.18b). This may

reflect fluid contributions from smectite-illite transition, the temperature window for which remains similar to that at 8 Ma (Fig. 5.18a). Gas migration is no longer significant at this stage.

According to [Cruz \(2018\)](#), during the Quaternary (the last c. 2.6 Ma), increasing sediment supply across the NW shelf drove gravity-driven syn-sedimentary deformation in response to higher sedimentation rates. This is consistent with our results along section A-B, where increased sediment flux from c. 2 Ma is recorded by a basinward shift of the slope break (Fig. 5.18c). Gravitational deformation resumed and intensified from 1.6-1.2Ma (Figs 5.16, 5.17, 5.18c). Faults F1 and F2 were abandoned for F3 and F4, which requires a migration of high pore pressure along the detachment. At the same time, overpressure on the overlying layers increases, and starts to be compartmentalized between normal faults F2-F4 (grey on Fig. 5.18c). The smectite-to-illite transformation window remains active along the sequences between detachment and the Amazon Fan series.

From 0.8 Ma to the present, continued sediment supply leads to further progradation of the slope break, now located between F3 and F4 (Fig. 5.18d). Normal faults F4 and F5 reach the seabed and form stepped scarps, showing that these faults remain active together with the frontal thrusts. To activate F4, pore fluid pressure along the fault needs to increase substantially. However, to activate F5, a strong decrease of the pore fluid pressure along F4 is required, attesting to a seaward migration of pore pressure. Within the sedimentary pile, overpressure continues to increase and remains compartmentalized by active faults. In terms of overpressure mechanisms, smectite-to-illite transition continues to represent an important secondary pore pressure mechanism within the fan.

Our modeling results suggest extremely high pore pressure along the detachment and the faults for all steps modeled of Amazon Fan. However, we cannot rule out that they are biased by the triggering of viscous deformation once a certain pore pressure threshold is reached ([Ings and Beaumont, 2010](#)). In any case, the pore pressure along the detachment

remains close to lithostatic and taking into account viscous deformation will not change the spatial and temporal evolution of the pore pressure in the Amazon fan.

V.6.2 Overpressure mechanisms in the Amazon Fan

Our results allow us to consider the roles of three potential pore pressure generation mechanisms within the SE compartment of the Amazon Fan: clay mineral transformation (smectite-to-illite); hydrocarbon generation from gas-prone source rocks ; and disequilibrium compaction (undercompaction) controlled by sedimentation rates.

From 8 Ma to the present-day, smectite-to-illite transition is found to take place within the sedimentary succession of the Amazon Fan mainly above the detachment (c. 69.7Ma) (Fig. 5.18). This result is consistent with an analysis of present-day pore pressure in well 1-BP-3-APS using the method of Bowers, which attests to the presence of a fluid expansion mechanism below depths of 3500m. The lower part of the transition window intersects the detachment in certain places (beneath the continental shelf and to seaward beneath the compressional domain), but not along the most active part of the detachment (between F1 and compressional domain), However, we cannot rule out that the temperature transition may have been located at the detachment level before 8 Ma, and that fluids generated were trapped near the detachment. Therefore, our results provide evidence for the smectite-to-illite transition at best being a possible early contributor to the generation of overpressures along the detachment.

The maturation of OAE source rocks and migration of thermogenic gas took place at least 16 Ma and up to 92 Ma before the onset of deposition of the Amazon Fan at 8 Ma (Fig. 5.14). In contrast to a previous study ([Cobbold et al., 2004](#)), a recent gas expulsion from Cenomanian-Turonian source rocks (equivalent to OAE2) at c. 6 Ma does not seem possible. Hydrocarbons migrated upward to be trapped in successions that in places lie at depths of hundreds meters beneath the detachment (Fig. 5.12, 5.18). The accumulation of

thermogenic gas beneath the detachment might have acted as an overpressure generating mechanism before the arrival of Amazon Fan (c. 8Ma), but there is no evidence of up-dip migration to the level of the detachment after that time. It appears that hydrocarbons would only be able to migrate upward to the detachment level or into overlying successions if there were structures present that breach the detachment. Thus, from 8 Ma to the present-day, our results provide no evidence of gas migration along the detachment (Fig. 5.12).

Our modeling results provide evidence of a downslope migration of the deformation caused by detachment overpressure during the progradation of the Amazon Fan during the last 8 Ma (Fig. 5.16, 5.17). We argue that disequilibrium compaction during the accumulation of up to 6 km of sediment has been the predominant overpressure mechanism along the detachment throughout the deposition of the Amazon Fan.

Sediment supply to the SE compartment of the Amazon fan decreased due to the migration of the sediments to the NW from 5.5 Ma, and deformation rates reduced to a minimum (Fig. 5.18b). From 2 Ma, when the sedimentation rate became massive, the basinward migration of the rapidly accumulating sediment load again induced disequilibrium compaction mechanisms. The migration of overpressure along the detachment led to high deformation rates.

At the present day, the SE compartment of the Amazon Fan continues to be characterized by some overpressure (Fig. 5.18d). According to our analysis of well 1-BP-3-APS, a pore pressure increase takes place below 3500 m and to at least 5500 m depth based on the method of Eaton (Fig. 5.7), while the method of Bowers points to fluid expansion mechanisms. Since no gas has been found in this interval, we favor clay mineral transformation, consistent with the depth of the smectite-to-illite temperature window (1500-6000 meters).

Biogenic gas might be acting as a present-day overpressure mechanism within the Amazon Fan succession. This gas generation could be related to a tertiary marine deltaic

source rocks (type II organic matter), related to supply from Amazon Fan, described by [Mello et al \(2000\)](#). Geochemical modeling applied to ODP site 938 at 2801.01 m water depth on the mid-fan indicates that sedimentation rates and organic carbon content within the upper 400 m are sufficient to drive *in situ* methanogenesis and lead to gas hydrate formation ([Arning et al., 2013](#)). On the NW fan, gas hydrates sampled from seafloor vents within the upper slope compressional belt are composed of methane isotopically consistent with a biogenic origin ([Ketzer et al., 2018](#)). In the subsurface, biogenic gas is reported on geochemical analysis of some wells in SE compartment (1APS-09-AP, 1-APS-14-AP, 1-APS-41-AP, 1-APS-51A-AP). Of the smaller number of wells drilled in the NW compartment, only one (1-APS-36-AP) shows evidence of biogenic gas. Results from well 1-BP-3-APS using the method of Bowers indicates fluid expansion mechanism at the present-day. If this fluid is gas, its origin might be biogenic.

In any case, the present-day overpressure conditions show that the SE compartment of the Amazon Fan is not at equilibrium and gravity driven deformation could occur at any time.

V.6.3 Implications for other deep-sea fans

The gravitational collapse of sedimentary successions above salt or shale detachments to generate syn-sedimentary tectonic belts is increasingly recognized as an aspect of continental margin evolution ([Rowan et al., 2004](#); [Morley et al., 2011](#)). Most of the world's major rivers culminate in deep-sea fans of kilometric thickness that contain evidence of collapse systems developed above overpressured shale detachments ([Morley et al., 2011](#)). The dynamics of these late Cenozoic depocentres have not previously been investigated using a modeling methodology as developed for our study, and we suggest that results from the Amazon fan provide possible insights into the functioning of other collapse systems.

The rapid deposition of deep-sea fans is thought to favor the development of overpressures within shale detachments by disequilibrium compaction, which may be supplemented by inflationary overpressures due to smectite-illite transition or hydrocarbon generation (Osborne and Swarbrick 1998; Morley et al., 2011). Our modeling results from the Amazon fan provide strong support for the role of disequilibrium compaction, both in generating overpressures within the detachment zone and in driving fault movements over time. Moreover, our results suggest that changes in sediment supply over time, and in space during the seaward progradation of the shelf-slope wedge, make the gravitational collapse of deep-sea fans a fundamentally episodic process, at the scale of the activity of the extensional-compressional system.

Our modeling results also support the role of clay mineral transformations in the development of overpressure within the thickening depocentre. However, the smectite-illite transition window remains mainly above the detachment during the growth of the fan, notably beneath all but the outermost part of the compressional system (Fig. 5.18), indicating it has not significantly influenced the dynamics of collapse. The position of the smectite-illite transition window is a consequence of rapid burial of the detachment, despite relatively low temperature gradients within the fan (Fig. 5.13). In general, geothermal gradients within deep-sea fans are relatively low due to thermal blanketing by rapid deposition of cold sediments (e.g. Wangen, 1995), but also depend on the underlying crustal heat flow. Thus slower sedimentation rates will raise thermal gradients (and the smectite-illite transition window), as will higher crustal heat flow. We infer that the possible role of clay mineral transformations on overpressures at detachment level will depend on the interplay of sedimentation rate with regional geothermal gradients. It would be of interest to test the role of clay mineral transformations within other deep-sea fans using our modeling technique.

Our results from the Amazon fan also indicate that gas does not influence overpressures at or above the level of the detachment, as thermogenically generated hydrocarbons remain trapped in the successions beneath the detachment (Fig. 5.18). This is

broadly consistent with an understanding of shale detachments as shear zones that act as barriers to the vertical migration of fluids (Brown et al. 1994). Nonetheless, fluids may be able to cross such barriers during tectonic movements, e.g. due to the formation of duplexes that incorporate underlying material (Moore & Vrolijk, 1992). Many deep-sea fans overlie deeper hydrocarbon systems and include evidence of thermogenic gas venting at seafloor (Loncke and Mascle, 2004; Ketzer et al., 2018), suggesting either that thermogenesis takes place above the detachment or that fault movements have breached the detachment. In the SE compartment of the Amazon fan, our results suggest it would be of interest to seek evidence of deep hydrocarbon leakage from seafloor vents above the duplexes at the leading edge of the compressional system (Fig. 5.18d).

V.7 CONCLUSIONS

In this study, we have investigated the main mechanisms of overpressure that contributed to the gravitational collapse of the Amazon fan during its growth over the last 8 Ma. The study is based on the structural restoration of a seismic profile across the Southwestern Amazon Fan, used to constrain numerical modeling of the evolution of pore pressure and temperature.

The modeling results indicate that disequilibrium compaction has been the predominant overpressure generation mechanism along the Amazon Fan detachment. Phases of gravity spreading and deformation at 8 Ma and after 2 Ma correlate to increase sediment flux to the deep-sea fan, whereas decreased flux to the SW Amazon fan from 5.5-3.7 Ma was accompanied by cessation of gravity spreading/deformation. This observation, coupled with our numerical modeling suggests that disequilibrium compaction is the dominant driving mechanism of overpressure in the Amazon Fan. Furthermore, from 2 Ma, progradation of the Amazon Fan drove the basinward migration of the deformation front, which modeling results show was matched by a downslope migration of overpressure along the detachment.

The modeling results also show that clay mineral transformations and hydrocarbon generation played secondary role in fluid overpressure generation. Fluids were generated by smectite-illite transition within the sedimentary succession of the Amazon Fan over the last 8 Ma. However, fluid release took place above the detachment surface throughout the growth and collapse of the fan. Modeling of hydrocarbon generation from oceanic anoxic events (source rocks) shows that hydrocarbon gas expulsion took place before the onset of deposition of the Amazon Fan and that the migrating fluids were trapped in strata beneath the detachment level.

Acknowledgments

The authors gratefully acknowledge the support granted during the completion of this study by Petrogal-Galp Brazil SA and CNPq (Brazilian National Research Council, grant agreement N°. 201531/2016-0), in the form of PhD scholarship made to Juliana M. Gonçalves de Souza. We also acknowledge the Brazilian Agência Nacional do Petróleo, Gás Natural e Biocombustíveis (ANP) for seismic and stratigraphic data made available to Universidade Federal Fluminense (UFF) and Universidade do Estado de Rio de Janeiro (UERJ). Daniel Praeg was supported by funding from the European Union's Horizon 2020 research and innovation program under Marie Skłodowska-Curie grant agreement No. 656821, and by the Brazilian Coordination of Superior Level Staff Improvement IODP /CAPES-Brazil (Edital 38/2014). Our special thanks are also due to Beicip-Franlab, Optum Computational Engineering and SMT Kingdom for the use of educational licenses. Finally, we would like to thank for all the suggestions and corrections made during the review process. Special thanks to MSc. Eduardo de Mio for his critical and insightful comments that much improved the quality of this paper. We also thank Alexandre Lethiers for diligently drafting all the figures included in this paper.

Appendix A – Pore pressure estimation from 1D Geomechanical model

Here we detail the methods of [Eaton \(1975\)](#) and [Bowers \(1995, 2001\)](#) and their application to estimating present-day pore pressures in well 1-BP-3-APS (Fig. 5.6). The two methods are based on different assumptions. Eaton's method assumes disequilibrium compaction (undercompaction) to be the main overpressure mechanism. However, with the transition zone into the overpressure zone in the BP-3-AP, the normal compaction trend (NCT), which means the trend of travel time property plotted as function of depth through the normal pressure data, shows the existence of deflection data trend (from 80 μ s/m to 150 μ s/m, see fig. 5.A1), representing possible overpressure due to fluid expansion mechanisms. [Bower's method \(1995, 2001\)](#) allows capturing the depth at which such fluid expansion mechanisms take place. We thus used this approach to evaluate the present-day pore pressure considering the mineral transformation, i.e., clay transformation and presence of gas. Density-acoustic crossplot from 1-BP-3-APS was used to identify unloading and shows clear unloading response.

A.1 - Eaton's Method

The [Eaton \(1975\) approach](#) is used to estimate abnormal pore pressure caused by compaction (disequilibrium compaction or under-compaction). Such compaction induces in-situ physical properties changes (compaction, porosity, and effective stress changes) and

variations of resistivity or transit time from the expected trend line are interpreted as overpressure (Eaton, 1972).

In this study, raw resistivity data was not available due to commercial sensitivity, we thus used sonic log data (Fig. 5.A1). The method includes a fudge factor, the Eaton coefficient, which enables the user to alter the trend line. An Eaton coefficient of 3.0 was established in the Gulf of Mexico (Eaton, 1975), and most trend-line pore pressure methods are variations of the method of Eaton (1975) with locally calibrated coefficients. The coefficient 3.0 was not altered for Amazon fan, due to absence of direct pressure measurements to account for overpressure mechanisms other than undercompaction.

We thus use Eaton’s equation (Fig. A1) :

$$P_p = \sigma_v - (\sigma_v - P_{hyd}) \left(\frac{\Delta t_n}{\Delta t_{log}} \right)^{3.0} \tag{Eq. A1}$$

where P is the pore pressure, σ_v is the overburden or vertical stress, P_{hyd} the hydrostatic pressure, Δt_n is the interval transit time of shale considering normal compaction trend and

Δt_{log} is the interval transit time obtained from well logging.

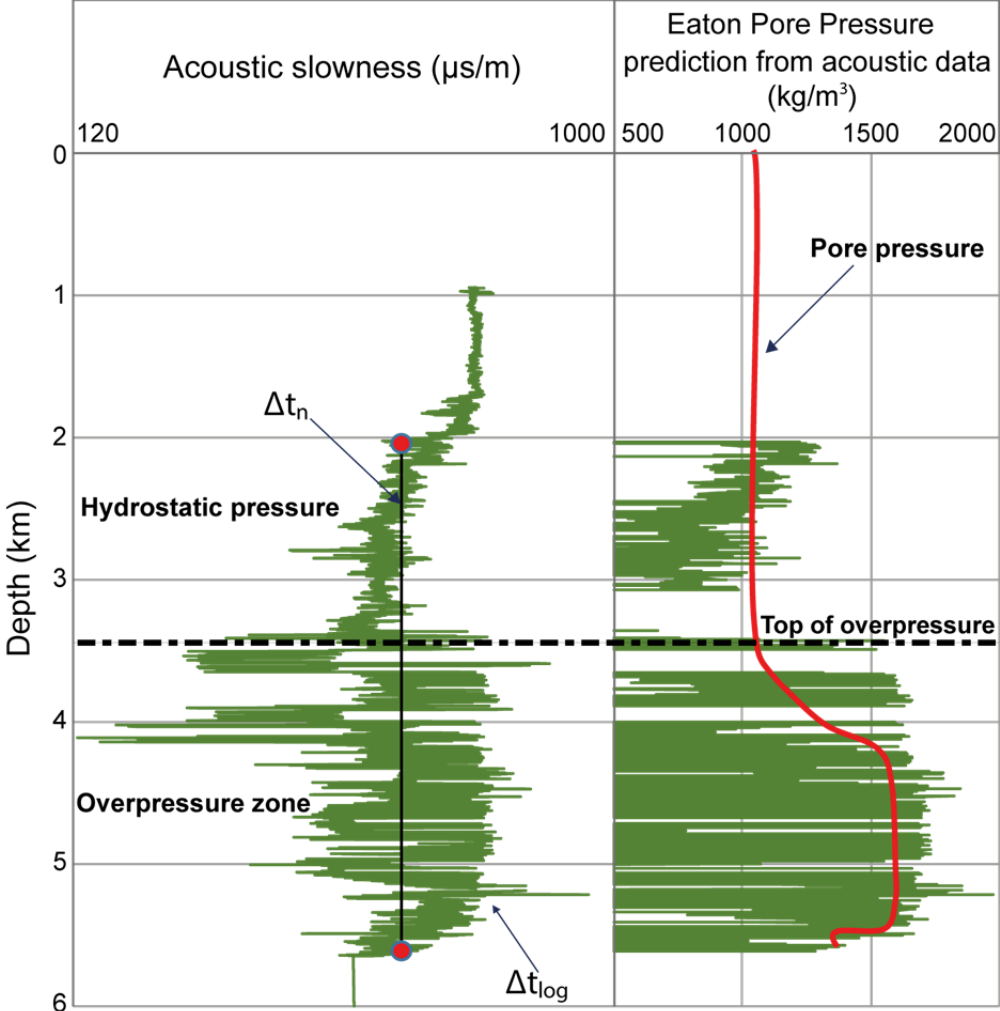


Figure 5.A1: Schematic plots showing: (1) left track, acoustic slowness from 1-BP-3-APS well, the normal compaction trend (*NCT*) of the transit time in the normal pressure condition (Δt_n) and pore pressure response to transit time (Δt_{log}); (2) right track, Eaton' pore pressure prediction from acoustic slowness using equation A1 (green log). Red line is final pore pressure interpretation.

A.2 - Bowers' Method

According to [Bowers \(1995\)](#), the depth at which excess pressure is generated by fluid expansion mechanisms can be captured from strain parameters such as velocity and density profiles. The effective stress can be retrieved from seismic interval velocities and pore fluid pressure deduced from overburden stress using Terzaghi's relationships ([Terzaghi, 1943](#)). This method captures mechanisms responsible for fluid pressure generation and provides pore pressure profiles from effective stress accounting for these mechanisms.

To capture the depth at which fluid expansion mechanisms might start unloading sediments, we cross-plot compressional velocity (from sonic log) and density to seek a

possible velocity reversal. Only densities and compressional velocities of mudstones and shales intervals were used to minimize the effect of lithology changes (Bowers, 1995, 2001). To do this, we applied a cut-off used the gamma ray log, assuming 65gAPI values for shales, 25gAPI for carbonates and 35gAPI for sandstones. Visual characterization of cuttings in the shakers are then compared with the gamma ray log to execute the cut-off procedure.

We apply Terzaghi's equation to calculate the effective stress (Terzaghi, 1943) and deduce the pore pressure. To do so, we first need to estimate the overburden stress. The magnitude of the total vertical stress (σ_v) is the weight of the overlying formations assuming relatively flat topography. σ_v is thus calculated from the integration of the density log:

$$\sigma_v = \int \rho g dz \quad (\text{Eq. A2})$$

with g is the gravitational acceleration in m.s^{-2} , ρ the rock density (kg.m^{-3}) and z depth (m).

Since logs are not run at shallow depths, density data were extrapolated to the surface for the upper sections using correlations of Gardner et al. (1974). Gardner's equation is an empirical equation that relates P-wave velocity to bulk density. This pseudo-velocity relationship is commonly used in estimating acoustic or density logs when only one of them is available. Gardner showed that:

$$\rho = \alpha V^\beta \quad (\text{Eq. A3})$$

where ρ is bulk density, V the compressional P velocity, and α and β empirically derived constant geology dependent. Gardner et al. (1974) proposed that one can obtain a good estimate of density in g.cm^{-3} , given velocity in ft/s , by taking $\alpha = 0.23$ and $\beta = 0.25$.

Assuming this, and using units of g.cm^{-3} , the equation is reduced to the following:

$$\rho = 0.23 V_p^{(0.25)} \quad \text{kg/m}^3 \quad (\text{Eq. A4})$$

To calculate the pore pressure, we then used velocity/effective stress relations established by Bowers (1995). Effective stresses are calculated from compressional transit

time and Terzaghi's equation is then used to derive pore pressure. In compaction disequilibrium conditions, outside the velocity reversal zone, [Bowers \(1995\)](#) proposed an empirical method to calculate the effective stress as follows:

$$V_p = V_0 + A\sigma_v'^B \quad (\text{Eq. A5})$$

where, V_p is the compressional velocity at a given depth and V_0 stands for the surface velocity (mudline velocity); σ_v' represents the vertical effective stress; A and B are the parameters which are calibrated with offset velocity and the effective stress data. V_0 is generally taken as 1520m/s that is the velocity near the sea floor.

The vertical effective stress can be expressed as:

$$\sigma_v' = \sigma_v - P_p \quad (\text{Eq. A6})$$

Where, σ' is the effective stress, σ_v is total vertical stress.

$$P_p = \sigma_v - ((V_p - V_0)/A)^{\frac{1}{B}} \quad (\text{Eq. A7})$$

The values $A = 10 - 20$ and $B = 0.7 - 0.75$ are taken from Gulf of Mexico (considering pressure in psi) and transit time fts^{-1} ($1ft\ s^{-1} = 0.3048m\ s^{-1}$ SI). Transit time is the inverse of velocity.

To address the effect of unloading effects, [Bowers \(1995\)](#) introduced an empirical correlation:

$$V = V_0 + A \left[\sigma_{\max} \left(\frac{\sigma_v'}{\sigma_{\max}} \right)^{\frac{1}{U}} \right]^B \quad (\text{Eq. A8})$$

Where, U is the unloading parameter, which is a measure of how plastic the sediment is. U represents the uplift of the sediment. 1 implies no permanent deformation and $U = \infty$ corresponds to a completely irreversible deformation.

$$\sigma'_{max} = \left(\frac{V_{max} - V_0}{A} \right)^{\frac{1}{B}} \quad (\text{Eq. A9})$$

σ'_{max} and V_{max} represent the values of vertical effective stress and velocity at the starting point, which are the maximal possible values, respectively (Bowers, 1995). The parameters A , B and U were obtained from Gulf of Mexico and Gulf Coast areas and works proposed by Bowers was developed using their well in the study area. The pore pressure for the unloading case can be estimated from:

$$P_{unl} = \sigma_v - \left(\frac{V_p - V_0}{A} \right)^{\frac{U}{B}} (\sigma_{max})^{1-U} \quad (\text{Eq. A10})$$

Where P_{unl} represents the pore pressure due to unloading behavior.

Appendix B - 2D mechanical model set-up

In this section, we present the mechanical rock properties estimated using the available log data from wells 1-BP-3-APS and 1-APS-31A-APS. These properties include internal friction angle and cohesion. Rock mechanical laboratory testing on core samples are the most accurate methods for estimation of rock strength, but they never can lead to a continuous profile of rock strength (Rabe et al., 2018, 2020; Chang et al., 2006) along wellbore and the tests were not executed on the study area. These parameters can be estimated using borehole as a continues source of rock strength to estimate internal friction and cohesion by using correlations of proposed in the literature based on acoustic data, that reflects the effect of lithology, porosity and fluid content.

B.1 - Internal friction angle

To calculate the Internal Friction Coefficient from sonic log, we used the *Lal V_p* correlation applicable to all types of lithology (Lal, 1999):

$$\mu = \tan(\arcsin((V_p - 1)/(V_p + 1))) \quad (\text{B.1})$$

where V_p is compressional velocity in *km/s*. Results are given in Table Supplementary material.

B.2 – Pore fluid pressure

The pore fluid pressure is taken into account through effective frictions defined as:

$$\mu_{eff} = \mu(1 - \lambda) \quad (\text{B.2})$$

With

$$\tau = \mu(1 - \lambda)\sigma_{normal} \quad (\text{B.3})$$

where τ and σ_{normal} are the shear and normal stresses, μ is the friction coefficient, and *Hubbert-Rubey* fluid pressure ratio λ (1959) is defined by

$$\lambda = \frac{P + \rho\omega gD}{|\sigma_z| + \rho\omega gD} \quad (\text{B.4})$$

with ρ and $\rho\omega$ being the wedge material and water densities, D is the water depth, σ_z is the stress perpendicular to the detachment and P is the pore pressure.

For each age, we took the maximum pore fluid pressure of each layer obtained during the basin modeling stage. Effective friction was then calculated from this pore fluid pressure and values for friction retrieved from the well data

B.3 – Cohesion

Cohesion (C_o) was retrieved from the unconfined strength (*UCS*) and the internal friction coefficient (μ). The *UCS* is the maximum axial compressive stress that a right-

cylindrical sample of material can withstand under unconfined conditions. To determine the UCS , we used correlations established as a function of V_p and lithologies.

For shales, claystones and mudstones, we relied on the [Horsrud \(2001\)](#) correlation defined as:

$$UCS = 1.35 * pow(V_p, 2.6) * 1.80, UCS \text{ in MPa} \quad (B.5)$$

For sandstones, we used the McNally equation ([McNally, 1987](#)):

$$UCS = 185165 * exp(-0.037 * \Delta t), UCS \text{ in psi.} \quad (B.6)$$

For limestones/carbonates, we used the Militzer equation ([Militzer and Stoll, 1973](#)), defined as:

$$UCS = pow((7682/\Delta t), 1.82), UCS \text{ in psi.} \quad (B.7)$$

Cohesion was estimated using equation 9 ([Jaeger et al., 2007](#)):

$$Co = \frac{UCS}{(2*\mu^2+1)+1} \quad (B.8)$$

References

Arning, T. E., Berk, v. W., Neto, E., S., Naumann, R., 2013. The quantification of methane formation in Amazon Fan sediments (ODP Leg 155, Site 938) by hydrogeochemical modeling solid – Aqueous solution – Gas interactions. *Journal of South American Earth Sciences*, vol 42, pp 205-215.

Arthur, M.A., Brumsack, H.-J., Jenkyns, H.C., and Schlanger, S.O., 1990. Stratigraphy, geochemistry, and paleoceanography of organic carbon-rich Cretaceous sequences. In Ginsburg, R.N., and Beaudoin, B. (Eds.), *Cretaceous Resources, Events and Rhythms*: Dordrecht (Kluwer), 75–119.

Berthelon, J., Yuan, X., Bouziat, A., Souloumiac, M. P., Cornu, T. and Maillot, B., 2018. Journal of Structural Geology, Vol 117, pages 148-162. <https://doi.org/10.1016/j.jsg.2018.08.003>

Brandão, J.A.S.L., Feijó, F.J., 1994. Bacia da Foz do Amazonas. Boletim de Geociências da Petrobrás 8, 91 - 99.

Bralower, T.J., Arthur, M.A., Leckie, R.M., Sliter, W.V., Allard, D.J., and Schlanger, S.O., 1994. Timing and paleoceanography of oceanic dysoxia/anoxia in the late Barremian to early Aptian. *Palaios*, 9:335–369.

Bruce, C. H., 1984. Smectite dehydration – its relation to structural development and hydrocarbon accumulation in northern Gulf of Mexico basin: AAPG Bulletin, v. 68, p.673-683.

Bolton, A.J. & Maltman, Alex & Clennell, M., 1998. The importance of overpressure timing and permeability evolution in fine-grained sediments undergoing shear. *Journal of Structural Geology*. 20. 1013-1022. [https://doi.10.1016/S0191-8141\(98\)00030-3](https://doi.10.1016/S0191-8141(98)00030-3)

Boullila, S., Brange, C., Cruz, A. M., Laskar, J., Gorini, C., Reis, T. and Silva, C. G., 2020 (in press). Astronomical pacing of Late Cretaceous third- and second-order sea-level sequences in the Foz do Amazonas Basin. Under review at *Marine and Petroleum Geology*.

Bowers, G. L., 1995. Pore Pressure Estimation from Velocity Data; Accounting for Overpressure Mechanisms Besides Undercompaction”, *SPE Drilling and Completions*, June.

Bowers, G. L., 2001. Determining an appropriate pore-pressure estimation strategy. *Offshore Technology Conference*, Houston, Texas, 30 April – 3 May.

Brown, K. M., Bekins, B., Clennell, B., Dewhurst, D. and Westbrook, G., 1994. Heterogeneous hydrofracture development and accretionary fault dynamics. *Geology*, vol 22, pp 259-262.

Burrus, J., 1998. Overpressure models for clastic rocks, their relation to hydrocarbon expulsion: a critical reevaluation, Law, B.E., G.F. Ulmishek, and V.I. Slavin eds., *Abnormal pressures in hydrocarbons environments: AAPG Memoir 70*, p. 35-63.

Callies, M., Darnault, R., Anka, Z., Le Garzic, E., Willien, F., Giboreau, R., 2017. A new kinematic tool for petroleum system modeling in complex structural settings: Application to the foothills region of Kurdistan. *The Geological Society – fold and thrust belts: structure style, evolution and exploration*.

Cardoso, R. A., and Hamza, V. M., 2007. Caracterizacao do campo térmico atual e evolucao térmica da Plataforma Continental do Estado do Rio de Janeiro. Conference paper, Sociedade Brasileira de Geofisica (SBGF).

Carman, P. C., 1937. Fluid flow through granular beds. *Transactions, Institution of Chemical Engineers, London*, 15: 150-166.

Carman, P. C., 1956. *Flow of gases through porous media*. Butterworths, London.

Chandra & Sekharaiah, D.S., Debnath, L., 1994. *Continuum Mechanics*. Academic Press, Inc.

Chang, C., Zoback, M. D., and Khaksar, A., 2006. "Empirical relations between rock strength and physical properties in sedimentary rocks." *Int. J. Pet. Sci. Eng.*, 51(3–4), 223–237.

Chenevert, M. E., and A.K. Sharma, 1991. *Permeability and effective pore pressure of shales: Society of Petroleum Engineers*, paper 21918.

Cobbold, P. R.; Rosselo, E. A., Vendeville, B. 1989. Some experiments on interacting sedimentation and deformation above salt horizons. *Bull. Soc. Géol. France*. 8 (3): 453 - 460.

Cobbold, P. R.; Mourges, R.; Boyd, K. 2004. Mechanism of thin-skinned detachment in the Amazon Fan: assessing the importance of fluid overpressure and hydrocarbon generation.

<https://doi.org/10.1016/j.marpetgeo.2004.05.003>

Cruz, A. M. 2018. Integrated geological and geophysical studies applied to understanding the evolution of the Offshore Amazon Basin. PhD thesis, Sorbonne University, France.

Cruz, A.M., Reis, A.T., Suc, J.P., Silva, C.G., Praeg, D., Granjeon, D., Rabineau, M., Popescu, S.M., Gorini, C., 2019. Neogene evolution and demise of the Amapá carbonate platform, Amazon continental margin, Brazil, Marine and Petroleum Geology. <https://doi.org/10.1016/j.marpetgeo.2019.04.009>

Cubas N, Souloumiac P, Singh, S. C., 2016. Relationship link between landward vergence in accretionary prism and tsunami generation. In Geology, Geological Society of America, vol. 44, p. 787-790.

Di Toro, G., Han, R., Hirose, T., DE Paola, N., Nielsen, S., Mizoguchi, K., Ferri, F., Cocco, M. & Shimamoto, T., 2011. Fault lubrication during earthquakes. Nature 471, 494–498 (2011). <https://doi.org/10.1038/nature09838>

[Dickey, P. A. 1971. Comment on Bayou Field, J. Pet. Technology, 22, 560-569.](#)

[Dickinson, G., 1953. Geological aspects of abnormal reservoir pressures in Gulf Coast, Louisiana: AAPG Bulletin, vol 61, pp. 2134-2142.](#)

Eaton, B. A., 1972. The effect of overburden stress on geopressure prediction from well logs. J. Pet. Technol. 24:929-934.

Eaton, B.A., 1975. The Equation for Geopressure Prediction from Well Logs, paper SPE 5544 presented at the 1975 SPE Annual Technical Conference and Exhibition, Dallas, TX, September 28 – October 1.

Erbacher, J., Mosher, D.C., Malone, M.J., et al., 2004. Proceedings of the Ocean Drilling Program, Initial Reports Volume 207.

Etris, E. L., Crabtree, N. J., Dewar, J., 2001. True depth conversion: more than a pretty picture. Scott Pickford, a core laboratories company. CSEG Recorder.

Figueiredo, J.J.P., Zalán, P.V., Soares, E.F., 2007. Bacia da Foz do Amazonas. Boletim de Geociências da Petrobrás 15, 299 - 309. Guimarães, P.T.M., Machado, E.R., Silva, S.R.P., 1989. Interpretação sísmo-estratigráfica em águas profundas na Bacia do Pará-Maranhão. In: Sintex, Seminário de Interpretação Exploratória, 1, Petrobras – Departamento de Exploração, Rio de Janeiro, Anais, 171 - 183.

Figueiredo, J., Hoorn, C., Van der Ven, P. and Soares, E., 2009. Late Miocene onset of the Amazon River and the Amazon deep-sea fan: Evidence from the Foz do Amazonas Basin: *Geology*, 37, p. 619–622.

Flood, R. D., Piper, D. J. W., Klaus, A., et al., 1995. Proceedings of the Ocean Drilling Program. Initial Reports 155.

Friedrich, O., Norris, R. D. and Erbacher, J., 2012. Evolution of middle to Late Cretaceous oceans — A 55 m.y. record of Earth's temperature and carbon cycle. *Geology*, 40, p. 107 – 110.

Gardner, G.H.F.; Gardner L.W.; Gregory A.R., 1974. Formation velocity and density -the diagnostic basics for stratigraphic traps. *Geophysics*. 39: 770–780.
<https://doi:10.1190/1.1440465>

Gorini, C., Haq, B.U., Reis, A.T., Silva, C.G., Cruz, A., Soares, E., Grangeon, D., 2014. Late Neogene sequence stratigraphic evolution of the Foz do Amazonas Basin, Brazil. *Terra Nova* 26, 179 - 185.

Grauls, D., 1999. Overpressure: Causal Mechanisms, Conventional and Hydromechanical Approaches. *Oil & Gas Science and Technology – Rev. IFP*, Vol.54, No.6, pp. 667-678.

Gutierrez, M. V., and Hamza, V. M., 2009. Campo Termico da Crosta na Regiao Sedimentar Bahia Sul e na Area Pre-Cambriana adjacente: Reavaliacao com base em dados corrigidos da Margem Continental. Conference paper. 11th International Congress of the Brazilian Geophysical Society held in Salvador, Brazil, August 24-28, 2009.

Hall, P.L., 1993, Mechanisms of overpressuring – an overview, in D.A.C. Manning, P.L. Hall and C.R. Hughes, eds., *Geochemistry of clay-pore fluid interactions*, Chapman and Hall, London, p. 265-315.

Hantschel, T., Kauerauf, A. I., 2009. *Fundamentals of Basin and Petroleum Systems Modeling*. Springer Dordrecht Heidelberg Berlin. p.3, 8, 31, 64.

Horn, C., Guerrero, J., Sarmiento, G.A. and Lorente, M.A., 1995. Andean tectonics as a cause or changing drainage patterns in Miocene northern South America: *Geology*, 23, p. 237–240, [https://doi.10.1130/0091-7613\(1995\)023<0237:ATAACF>2.3.CO;2](https://doi.10.1130/0091-7613(1995)023<0237:ATAACF>2.3.CO;2)

Horn, C., Bogotá-A, G.R., Romero-Baez, M., Lammertsma, E.I., Flantua, S.G.A., Dantas, E.L., Dino, R., do Carmo, D.A., and Chemale, F., 2017, The Amazon at sea: Onset and stages of the Amazon River from a marine record, with special reference to Neogene plant turnover in the drainage basin: *Global and Planetary Change*, v. 153, p. 51–65, <https://doi.10.1016/j.gloplacha.2017.02.005>

Horn, C., Wesselingh, F.P., ter Steege, H., Bermúdez, M.A., Mora, A., Sevink, J., Sanmartín, I., Sanchez-Meseguer, A., Anderson, C.L., Figueiredo, J.P., Jaramillo, C., Riff, D.D., Negri, F.R., Hooghiemstra, H., Lundberg, J., Stadler, T., Särkinen, T., Antonelli, A., 2010. Amazonia through time: Andean uplift, climate change, landscape evolution and biodiversity. *Science* 330:927–931. <http://dx.doi.org/10.1126/science.1194585>

Horsrud, P., 2001. Estimating mechanical properties of shale from empirical correlations. SPE Drill. Complet. 16, 68–73.

Hooper, R. J.; Fitzsimmons, R. J.; Grant, N.; Vendeville, B. C., 2002. The role of deformation in controlling depositional patterns in the south-central Niger Delta, West Africa. Journal of Structural Geology. 24: 847-859.

Hower, J., Eslinger, E. V., Hower, M. E. & Perry, E. A., 1976. Mechanism of burial and metamorphism of argillaceous sediment: mineralogical and chemical evidence. Geological Society of America bulletin, 87, 725-737.

Hubbert, M.K. and Rubey, W. W., 1959. Role of fluid pressure in mechanics of overthrust faulting: Mechanics of fluid-filled porous solids and its application to overthrust faulting. Bulletin of the Geological Society of America, vol. 70, pp. 115-166.

Ings, S.J., and Beaumont, C., 2010. Continental margin shale tectonics: preliminary results from coupled fluid-mechanical models of basin scale delta instability. J. Geol. Soc. 167, 571–582.

Jaeger, J.C., Cook, N. G., & Zimmerman, R., 2007. Fundamentals of rock mechanics. Wiley and Sons. Chicago.

Ketzer, J. M., Augustin, A., Rodrigues, L., Oliveira, R., Praeg, D., Pivel, M. A., Reis, A. T., Silva, C., and Leonel, B., 2018. Gas seeps and gas hydrates in the Amazon deep-sea fan. Geo-Marine Letters. DOI: <https://10.1007/s00367-018-0546-6>

Kozeny, I., 1927. Ueber kapillare Leitung des Wassers im Boden. Sitzungsber Akad. Wiss. Wien, 136(2a): 271-306.

Krabbenhoft, K. 2017. OptumG2 Theory. Optum Computational Engineering.

Kuncoro, A. K., Cubas, N., Singh, S. C., Etchebes, M., Tapponnier, P., 2015. Tsunamigenic potential due to frontal rupturing in the Sumatra locked zone. *Earth and Planetary Science Letters*, v.432, p. 311-322. <https://doi.org/10.1016/j.epsl.2015.10.007>

Lal, M. 1999. Shale stability: drilling fluid interaction and shale strength. SPE Latin American and Caribbean Petroleum Engineering Conference held in Caracas, Venezuela.

Law, B.E., J.R. Hatch, G.C. Kukal, and C.W. Keighin, 1983. Geological implications of coal dewatering: *AAPG Bulletin*, v.67, p. 2250-2260.

Law, B.E., and C.W. Spencer, 1998, Abnormal pressures in hydrocarbon environments, in Law, B.E., G.F. Ulmishek, and V.I. Slavin eds., *Abnormal pressures in hydrocarbons environments: AAPG Memoir 70*, p.1-11.

Loncke, L. and Mascle, J., 2004. Mud volcanoes, gas chimneys, pockmarks and mounds in the Nile deep-sea fan (Eastern Mediterranean): geophysical evidences. *Marine and Petroleum Geology*, vol 21, issue 6, pp 669-689. <https://doi.org/10.1016/j.marpetgeo.2004.02.004>

Maillot, B. and Leroy, Y. M., 2006. Kink-fold onset and development based on the maximum strength theorem. *J. Mech. Phys. Solids* 54, 2030–2059, <https://dx.doi.org/10.1016/j.jmps.2006.04.004>

Maltman, A. J. and Bolton, A., 2003. How sediments become mobilized. From: Van Rensbergen, R., Lis, R.R., Maltman, A.J. & Morley, C.K. (eds) 2003. *Subsurface Sediment Mobilization*. Geological Society, London, Special Publications, 216, 9-20. <https://doi.10.1144/GSL.SP.2003.216.01.02>

Marsden, D., 1989. Layer cake depth conversion in *Seismic Interpretation 13 series*. Amoco (UK) Exploration Company. London, England.

Matos, R. M. D., 2000. Tectonic evolution of the equatorial South Atlantic. In: Mohriak, W.U., Talwani, M. (Eds.). Atlantic rifts and continental margins, AGU Geophysical Monograph 115, 331 - 354.

McNally, G.H., 1987. Estimation of coal measures rock strength using sonic and neutron logs. *Geoexploration* 24, 381–395.

McKenzie, D., 1978. Some remarks on the development of sedimentary basins. *Earth and Planetary Science Letters*. Vol 40, issue 1, p. 25-32. [https://doi.org/10.1016/0012-821X\(78\)90071-7](https://doi.org/10.1016/0012-821X(78)90071-7)

Meade, R.H., 1994. Suspended sediments of the modern Amazon and Orinoco rivers: *Quaternary International*, 21, p. 29–39.

Mello, M. R., 1988. Geochemical and molecular studies of the depositional environments of source rocks and their derived oils from the Brazilian marginal basins. Ph.D. Thesis, Bristol University, 240pp.

Mello, M. R., Mosmann, M.R., Sylva R., Maciel, R.R., and Maranda, R.P., 2000. Foz do Amazonas Area: the last frontier for elephant hydrocarbon accumulation in the South Atlantic realm. Second Wallace E. Pratt memorial Conference on Petroleum Provinces of the 21st Century, San Diego, California, January 12-15, 2000. AAPG.

Mesri, G., and Olson, R. E., 1971. Mechanisms controlling the permeability of clays, *Clays Clay Miner.*, 19, 151-158.

Militzer, H., Stoll, R., 1973. Einige Beitrageder geophysics zur primadatenerfassung im Bergbau, *Neue Bergbautechnik*. Lipzig 3, 21–25.

Miranda, F.P., Bentz, C.M., Beisl, C.H., Lorenzetti, J.A., Araújo, C.E.S., and Silva, Jr., C.L., 1998. Application of Unsupervised Semivariogram Textural Classification of RADARSAT-1

data for the detection of natural oil seeps offshore the Amazon Mouth: proceedings of the Radarsat Adro Symposium, CD-ROM format.

Moore, C. J. and Vrolijk, P., 1992. Fluids in accretionary prisms. American Geophysical Union, pp 113-135.

Moos, D., Peska, P., Finkbeiner, T. and Zoback, M., 2003. Comprehensive wellbore stability analysis utilizing Quantitative Risk Assessment. Journal of Petroleum Science and Engineering. Vol. 38, Issues 3–4, pp. 97-109. [https://doi.org/10.1016/S0920-4105\(03\)00024-X](https://doi.org/10.1016/S0920-4105(03)00024-X)

Morley, C. K. and Guerin, G., 1996. Comparison of gravity - driven deformations styles and behavior associated with mobile shales and salt tectonics. Tectonics. 15: 1154 - 1170. <https://doi.org/10.1029/96TC01416>

Morley, C. K., King, R., Hillis, R, Tingay, M. and Backe, G., 2011. Deepwater fold and thrust belt classification, tectonics, structure and hydrocarbon prospectively: A review. Earth-Science Reviews, vol 104, issues 1-3, pages 41-91. <https://doi.org/10.1016/j.earscirev.2010.09.010>

Mourgues, R., Lecomte, E., Vendeville, B., Raillard, S., 2009. An experimental investigation of gravity-driven shale tectonics in progradational delta. Tectonophysics 474, p. 643-656.

Nashaat, M., 1998, Abnormally high fluid pressure and seal impacts on hydrocarbon accumulations in the Nile Delta and North Sinai Basins, Egypt, in Law, B.E., G.F. Ulmishek, and V.I. Slavin eds., Abnormal pressures in hydrocarbon environments: AAPG Memoir 70, p. 161–180.

Oliveira, V., 2005. A Tectônica Gravitacional do Cone do Amazonas: Compartimentação estrutural e mecanismos controladores. Tese de Mestrado. Universidade Federal Fluminense.

Oliveira V., Reis A. T. and Silva, C.G., 2005. Fatores condicionantes da tectonica gravitacional no Cone do Amazonas. In: Ninth International Congress of the Brazilian Geophysical Society, 2005, Salvador. Ninth International Congress of the Brazilian Geophysical Society. Rio de Ja-neiro: Sociedade Brasileira de Geofisica – SBGf, CD-ROM, p. 1–6.

Oliveira, M. J. R ., Zalan P. V., Caldeira J. L., Tanaka A., Santarem P., Trosdorf Jr. I., and Moraes A., 2011. Linked extensional-compressional tectonics in gravitational systems in the Equatorial Margin of Brazil, in D. Gao, ed., Tectonics and sedimentation: Implications for petroleum systems: AAPG Memoir 100, p. 1 – 18.

Osborne, M.J. and Swarbrick, R.E. 1997. Mechanisms for generating overpressure in sedimentary basins: A reevaluation. AAPG Bulletin, 81, 1023-1041.

Penteado, H.L.B., Behar, F., Lorant, F., Oliveira, C.C., 2007 (in press). “Study of biodegradation process along the Carnaubais trend, Potiguar basin (Brazil) – Part 2”. Organic Geochemistry, pp. 15.

Perovano, R.J.S., Reis, A.T., Silva, C.G., Vendeville, B.C., Gorini, C., Oliveira, V. & Araujo, E.F.S. 2009. O processo de colapso gravitacional da secao marinha da Bacia da Foz do Amazonas – Margem Equatorial Brasileira. Revista Brasileira de Geofisica (2009) 27(3): 459-484.

Perovano, R.J.S., Vendeville, B.C., Reis, A.T., Silva, C.G., Gorini, C., Araujo, E.F.S. 2011. Modelagem fisica experimental de mecanismos de dedormação gravitacional simulando multiplos intervalos superpressurizados : APLICação à Bacia da Foz do Amazonas. Revista Brasileira de Geofisica (2011) 29(3): 583-607.

Rabe, C., Silva, G. A. F., Nunes, A.L.L.S. & Silva, C., 2018. Development of a New Correlation to Estimate the Unconfined Compressive Strength of a Chicontepec Formation. International Journal of Geomechanics. 18. [https://10.1061/\(ASCE\)GM.1943-5622.0001134](https://10.1061/(ASCE)GM.1943-5622.0001134)

Rabe, C., Perdomo, P., Roux, P., Silva, C. & Gambôa, L., 2020. Coupled fluid flow and geomechanics: a case study in Faja del Orinoco. Springer Series in Geomechanics and Geoengineering. 6. 23. <https://10.1007/s40948-019-00136-x>

Reis, A.T., Perovano, R., Silva, C.G., Vendeville, B.C., Araujo, E., Gorini, C., Oliveira, V., 2010. Two-scale gravitational collapse in the Amazon Fan: a coupled system of gravity tectonics and mass-transport processes. *J. Geol. Soc. Lond.* 167, 593-604.

Reis A.T., Araújo E., Silva C. G., Cruz A. M., Gorini C., Droz L., Migeon S., Perovano R., King I., Bache F. 2016. Effects of a regional décollement level for gravity tectonics on late Neogene-Quaternary large - scale slope instabilities in the Foz do Amazonas Basin, Brazil. *Marine and Petroleum Geology*.

Requejo, G., Sassen, R., Ukpabio, E., Kennicutt II, M. C., McDonald, T., Denous, M. C., and Brooks, J. M., 1995. Hydrocarbon source facies in the Niger Delta petroleum province as indicated by the molecular characteristics of oil. *Book of Abstracts, 1995 International Chemical Congress of Pacific Basins Societies, Honolulu, Hawaii, December 17-22, Inor. 7, 180.*

Rimington, N., Cramp, A. and Morton, A., 2000. Amazon Fan sands: Implications for provenance: *Marine and Petroleum Geology*, 17, p. 267–284.

Rowan, M. G., Peel, F. J. and Vendeville, B. C., 2004. Gravity-driven fold belts on passive margins. In: K. R. McClay. *Thrust tectonics and petroleum system: AAPG Memoir 82.*

Saffer, D. M., Marone, C., 2003. Comparison of smectite-and illite-rich gouge frictional properties: application to the updip limit of the seismogenic zone along subduction megathrusts. *Earth and Planetary Science Letters* 215 (1–2), 219–235.

Salençon, J., 2002. *De l'Elasto-Plasticité au Calcul à la Rupture*. Ellipses, Paris. 264 pp.

Silva, S.R.P., Maciel, R.R. & Severino, M.C.G 1999. Cenozoic tectonics of Amazon Mouth Basin. *Geo-Marine Letters*, 18, 256-262.

Silva, R., Reis, A.T., Silva, C.G., Vendeville, B., Gorini, C., Araújo, E.F.S., 2009. O processode colapso gravitacional e a estruturação da seção marinha da bacia da Foz do Amazonas - Margem equatorial brasileira. *Rev. Bras. Geofís.* 27, 459e484.

Swarbrick and Osborne, 1998. Mechanisms that generate abnormal pressures: an overview, in Law, B.E., G.F. Ulmishek, and V.I. Slavin eds., *Abnormal pressures in hydrocarbon environments: AAPG Memoir 70*, p.13-34

Terzaghi, K., *Theoretical Soil Mechanics*, 1943.

Tremblin, M.; Hermoso, M.; Minoletti, F., 2016. Eocene-Oligocene sea surface temperature and pCO₂ estimates. *PANGAEA*, <https://doi.org/10.1594/PANGAEA.865323>.

Thurrow, J., Brumsack, H.-J., Rullkötter, J., Littke, R., and Meyers, P., 1992. The Cenomanian/Turonian boundary event in the Indian Ocean—a key to understand the global picture. In Duncan, R.A., Rea, D.K., Kidd, R.B., von Rad, U., and Weissel, J.K.(Eds.), *Synthesis of Results from Scientific Drilling in the Indian Ocean*. *Geophys. Monogr.*, Am. Geophys. Union, 70:253–273.

Vendeville, B. C., and Cobbold, P. R., 1987. Glissements gravitaires synsedimentaires et failles normales listriques: modèles expérimentaux. *Comptes Rendus de l'Académie des Sciences de Paris*.1313 - 1319.

Wangen, Magnus. (1995). The blanketing effect in sedimentary basins. *Basin Research*. 7. DOI: <https://283-298.10.1111/j.1365-2117.1995.tb00118.x>

Watts, A. B., Rodger, M., Pierce, C., Greenroyd, C. J. and Hobbs and R. W., 2009. Seismic structure, gravity anomalies and flexure of the Amazon continental margin, NE Brazil. *Journal of Geophysical Research*, Vol. 114, B07103. <https://doi:10.1029/2008JB00625>

Wolff, B. and Carozzi, A.V., 1984. Microfacies, depositional environments, and diagenesis of the Amapá carbonates (Paleocene-Middle Miocene), Foz do Amazonas basin, offshore NE Brazil: Petrobras, Rio de Janeiro.

Wu, J. E., McClay, K., Frankowicz, E., 2015. Niger Delta gravity-driven deformation above the relict Chain and Charcot oceanic fracture zones, Gulf of Guinea: Insights from analogue models. Marine and Petroleum Geology, Vol. 65, p. 43-62.
<https://doi:10.1016/j.marpetgeo.2015.03.008>

Yuan, X. P., Leroy, Y. M. and Maillot, B., 2017. Reappraisal of gravity instability conditions for offshore wedges: consequences for fluid overpressures in the Niger Delta. Geophysical Journal International 208, 1665-1671. <https://doi:10.1093/gji/ggw474>

Yuan, X. P., Leroy, Y. M. and Maillot, B., 2020. Control of fluid pressures on the formation of listric normal faults. Earth and Planetary Science Letters, 529, 115849.
<https://doi.org/10.1016/j.epsl.2019.115849>

Zoback, M. D., 2007. Reservoir Geomechanics, University Press, Cambridge

Software:

JewelSuite Geomechanics (Baker Hughes)

<https://www.bhge.com/digital/field-planning-optimization/jewelsuite-geomechanics>

[OpenFlow Suite 2019](#)

<http://www.beicip.com/openflow-suite-2019>

[OptumG2 2018](#)

<https://optumce.com/products/optumg2/>